Accepted for publication in ApJ, 05-Dec-2005
Preprint typeset using LaTeX style emulateapj v. 6/22/04

arXiv:astro-ph/0512203v1 7 Dec 2005

DETECTING FAINT GALAXIES BY STACKING AT 24 μm

X. Z. Zheng[1], Eric F. Bell[1], Hans-Walter Rix[1], Casey Papovich [2], Emeric Le Floc'h [2,3], G. H. Rieke[2], and P. G. Pérez-González[2]

Accepted for publication in ApJ, 05-Dec-2005

ABSTRACT

We stack *Spitzer* 24 μm images for $\sim$ 7000 galaxies with $0.1 \leq z < 1$ in the Chandra Deep Field South to probe the thermal dust emission in low-luminosity galaxies over this redshift range. Through stacking, we can detect mean 24 μm fluxes that are more than an order of magnitude below the individual detection limit. We find that the correlations for low and moderate luminosity galaxies between the average $L_{\rm IR}/L_{\rm UV}$ and rest-frame B-band luminosity, and between the star formation rate (SFR) and $L_{\rm IR}/L_{\rm UV}$, are similar to those in the local Universe. This verifies that oft-used assumption in deep UV/optical surveys that the dust obscuration–SFR relation for galaxies with SFR $\leq 20\,{\rm M}_{\odot}\,{\rm yr}^{-1}$ varies little with epoch. We have used this relation to derive the cosmic IR luminosity density from $z = 1$ to $z = 0.1$. The results also demonstrate directly that little of the bolometric luminosity of the galaxy population arises from the faint end of the luminosity function, indicating a relatively flat faint-end slope of the IR luminosity function with a power law index of 1.2 ± 0.3.

Subject headings: galaxies: evolution — galaxies: general — infrared: galaxies

1. INTRODUCTION

The rapid decay of the cosmic mean star formation rate (SFR) density from $z = 1$ to the present epoch has been convincingly established over the last decade (see, e.g., Hopkins 2004 and references therein). The focus has now turned to characterizing the types of galaxies responsible for this decay. Rest-frame ultraviolet (UV) and optical emission-line studies indicate the decay since z $\sim$ 1 is strongly influenced by the behavior of the relatively low-mass galaxies (e.g., Brinchmann & Ellis et al. 2000; Juneau et al. 2005; Bundy et al. 2005; Bauer et al. 2005; Wolf et al. 2005). On the other hand, surveys in the thermal infrared (IR) have found many galaxies of intermediate and high mass with intense, deeply obscured star formation (Franceschini et al. 2003; Zheng et al. 2004; Bell et al. 2005; Pérez-González et al. 2005; LeFloc'h et al. 2005). However, the role of obscured star formation in lower-mass galaxies remains unknown (although see Heavens et al. 2004 for a powerful and complementary approach).

Among the many observational SFR estimators (see Kennicutt 1998a for a review), at high redshifts UV radiation is the most easily measured proxy for the SFR. It provides the basis for much of our understanding of the evolution of the cosmic SFR density (e.g., Madau et al. 1996; Steidel et al. 1999; Sullivan et al. 2000; Hopkins et al. 2001; Schiminovich et al. 2005). Yet, young stars are usually born in dust-rich environments; the dust absorbs the vast majority of the UV light and re-radiates this energy in the thermal IR. Therefore, to obtain a complete census of the bolometric luminosity from young stars, observations in both the UV and IR are required (see, e.g., Gordon et al. 2000). However, the available infrared facilities have lacked the sensitivity and imaging resolution to explore obscured star formation in low-luminosity, relatively low-mass galaxies, except for nearby examples. Thus, indirect estimates have had to be used for the IR outputs of such galaxies even at moderate redshift, using tools such as the empirical calibration of UV color to extinction (e.g., Meurer et al. 1999; Calzetti & Heckman 1999), or the locally-observed trend between $L_{\rm IR}/L_{\rm UV}$ and luminosity (showing that more luminous galaxies tend to have higher extinction; e.g., Wang & Heckman 1996; Bell 2003; Buat et al. 2005). These approaches have been applied to observations of high-redshift galaxies to derive the SFR per unit comoving volume (e.g., Adelberger & Steidel 2000; Hopkins 2001).

The goal of this paper is to measure directly the average IR outputs of low-luminosity galaxies at intermediate redshift. We use a deep 24 μm map of the Chandra Deep Field South (CDFS) from the Multiband Imaging Photometer on *Spitzer* (MIPS: Rieke et al. 2004). The 24 μm map is limited by both photon and confusion noise (Dole et al. 2004). We find that stacking on the position of known intermediate redshift galaxies substantially reduces both sources of noise, allowing secure detection of average flux densities substantially below the conventional confusion limit. We have stacked 24 μm images of several thousand intermediate- and low-luminosity galaxies at $0.1 \leq z < 1$. We combine the resulting detections with the COMBO-17 data set to investigate the effects of dust obscuration in galaxies with $m_R < 24$ mag out to $z \sim 1$. We find no evidence for evolution in the relationship between obscuration and the SFR over this range of redshift. Our results suggest that the IR luminosity function has a relatively flat slope (power law index of 1.2 ± 0.3) toward low luminosities, at least out to $z \sim 1$.

The paper is organized as follows. Section 2 describes the data and the selection of the galaxy sample. Section 3 addresses the methods for stacking the images and describes tests of their validity. Section 4 shows the results. Section 5 uses these results to refine estimates of the cos-

---

[1] Max-Planck Institut für Astronomie, Königstuhl 17, D-69117 Heidelberg, Germany
[2] Steward Observatory, University of Arizona, 933 N Cherry Ave, Tucson, AZ 85721, USA
[3] GEPI, Observatoire de Paris-Meudon, 92195 Meudon, France
Electronic address: zheng@mpia.de

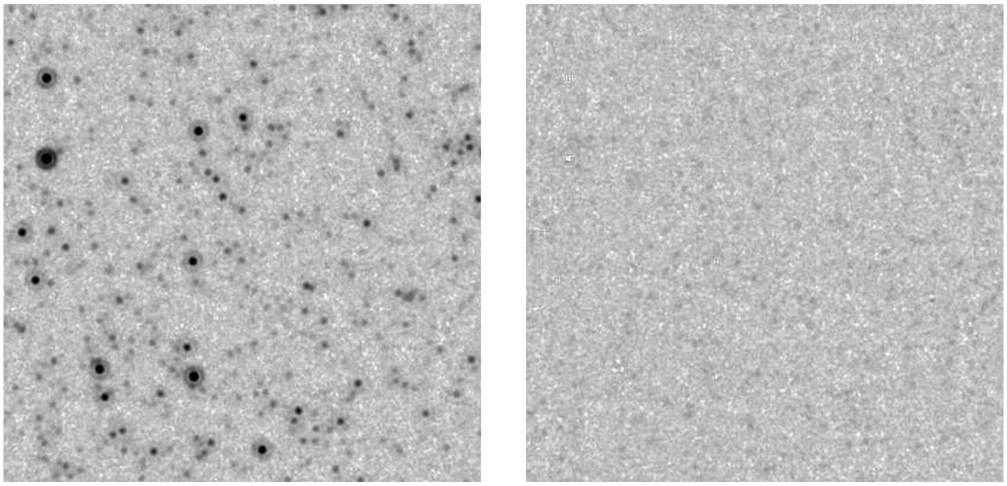

FIG. 1.— Illustration of Spitzer/MIPS 24 μm images before and after PSF subtraction of individually-detected sources. *Left*: an image section ($10' \times 10'$) in the CDFS; *Right*: the corresponding residual image after removing all detected sources brighter than 83 μJy (at the 80% completeness). Two images are shown in the same greylevel scale. Sources seen in the residual images are fainter than 83 μJy.

mic SFR density from z $\sim$ 1 to the present epoch. Our work is summarized in Section 6. Throughout the paper we adopt a cosmology with $H_0 = 70\,\mathrm{km\,s^{-1}\,Mpc^{-1}}$, $\Omega_\mathrm{M} = 0.3$ and $\Omega_\Lambda = 0.7$.

2. THE DATA AND GALAXY SAMPLE

In this paper, we combine ground-based optical data from the COMBO-17 photometric redshift survey with 24 μm data from MIPS on board the Spitzer Space Telescope. As part of COMBO-17, the extended CDFS (centered on $\alpha_{2000} = 03^h32^m25^s$, $\delta_{2000} = -27°48'50''$) was imaged in 5 broad and 12 medium-band optical filters from 350 to 930 nm (Wolf et al. 2003). The CDFS catalog is available for public use (Wolf et al. 2004). The catalog presents astrometry and photometry for 63501 objects in an area of $30'.5 \times 30'$. Of these, photometric redshifts and rest-frame luminosities in the standard Johnson U, B, V bands and a synthetic UV band centered at 280 nm[4] are measured for $\sim$9 000 classified galaxies with aperture magnitudes $m_R < 24$ mag and $z < 1.1$. Redshift uncertainties have been tested against large spectroscopic datasets and are $\delta z/(1+z) \sim 0.02$ at the median galaxy magnitude of $R \sim 22$; astrometric uncertainties are $\sim 0.1''$ (Wolf et al. 2004).

MIPS observations of the CDFS at 24 μm were performed under MIPS Guaranteed Time Observations (GTOs). A rectangular field of $90' \times 30'$ was observed in slow scan-map mode, with a total integration time of $\sim$ 1380 seconds per pixel. The 24 μm image reduction was done with the MIPS Data Analysis Tool (Gordon et al. 2005). A final mosaic image was produced with resolution $1''.25$ per pixel and a Point-Spread Function (PSF) with Full Width at Half Maximum (FWHM) $\simeq 6''$. We used Sextractor (Bertin & Arnouts et al. 1996) for source detection. Because the typical size of an intermediate redshift galaxy is $\ll 6''$, we chose to fit all galaxies as unresolved point sources. The few clearly extended sources were individually analyzed. An empirical PSF was built by stacking 18 bright point sources; this PSF was subsequently used for PSF fitting within $10''$ of all other objects[5]. The ALLSTAR routine in IRAF's DAOPHOT was used to simultaneously fit multiple sources to the entire 24 μm image mosaic. Local background values were estimated to be the mode value of an annulus with an inner radius of $17''$ (5 FWHM) and width $20''$ centered on a given target[6]. The brightest sources were fit first and then removed. The fainter sources hidden by the brightest sources were then detected and progressively included into ALLSTAR fitting. The flux of each detected object is derived from the PSF fits. We cut the 24 μm catalog at the 80% completeness level of 83 μJy ("5σ", see Papovich et al. 2004 for the description of the completeness limit; the Papovich et al. catalog is very similar to that described here to within the errors).

The MIPS and COMBO-17 areas on the sky do not completely overlap. For the present analysis, we choose the subsample of galaxies contained within both the MIPS and the COMBO-17 areas, avoiding the edges in the MIPS data. This sample covers an area of $\sim$800 arcmin^2 and contains 9785 objects with $m_R < 24$ (of which 7892 are galaxies in the redshift range $0.1 \leq z < 1$). Before the core analysis of this paper, we constructed a catalog of 24 μm detected sources that could be matched to COMBO-17 sources with redshifts. We cross-correlated the two catalogs with a tolerance of $1''.25$, or 3σ positional uncertainty, as estimated from bright stars and compact sources. Of the 9785 COMBO-17 objects at $m_R < 24$, 1725 objects are MIPS 24 μm resolved sources. Of these, 1352 objects are selected in our sample as galaxies in the redshift range $0.1 \leq z < 1$.

---

[4] The synthetic 280 nm passband has a square bandpass and 40 nm FWHM. Rest-frame luminosities in the 280 nm bandpass are extrapolated using the best-fit galaxy templates for galaxies with $z \lesssim 0.3$. Rest-frame luminosities in U- and B-band are always interpolated in the redshift range of interest, whereas V-band luminosities are extrapolations for galaxies with $z \gtrsim 0.7$.

[5] Aperture corrections from this empirical PSF are similar to the updated PSFs in the "Spitzer Space Telescope Multiband Imaging Photometer for Spitzer (MIPS) Data Handbook" (version 2.3) to within the errors.

[6] The use of median or mean values for the sky would make little difference for uncrowded sources; the mode is adopted as it is substantially more outlier-resistant than either mean or median in the case of sky annuli contaminated by sources.

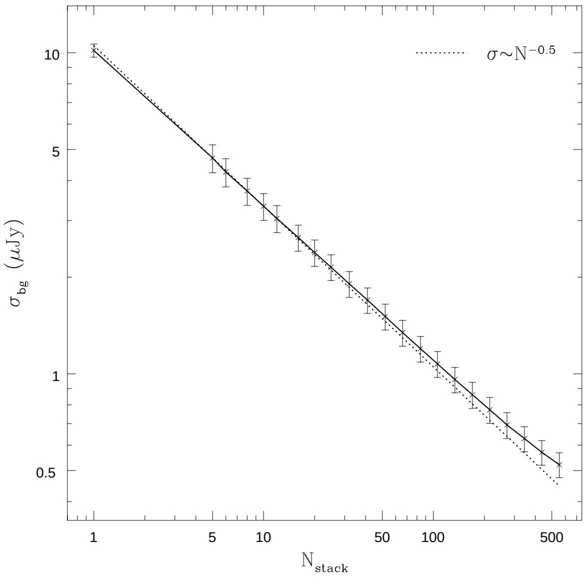

FIG. 2.— Reduction of the background RMS with increasing number of stacked images. Here σ_{bg} refers to the RMS of the flux within an aperture of radius 5″. For comparison, the dotted line shows the inverse square root of the stack number, normalized to the measured σ_{bg} at $N_{stack} = 10$.

3. MIPS 24 μM IMAGE STACKING

In this section we describe the specifics of deriving the mean 24 μm fluxes for galaxy sub-sets through stacking. Basically, there are three steps: first, the removal of all individually-detected sources in the image; second, the stacking of the residual image postage stamps through averaging or medianing; finally, the addition of the individual 24 μm fluxes for all MIPS sources that coincide with the optical positions of the galaxy sub-set at hand.

3.1. *Stacking: method and testing*

Deep Spitzer surveys at 24 μm, including these data, are limited by a combination of photon noise and confusion noise (Dole et al. 2004). The confusion noise at a given position on the sky is related to the unresolved extragalactic population; increasing exposure time will not reduce this source of noise and therefore it sets a limit to one's ability to individually detect galaxies in Spitzer 24 μm observations. However, the confusion noise does vary across the sky. If one is interested in estimates of the average flux for classes of objects (e.g. galaxies at a given redshift) with known coordinates, one can improve the detection threshold by stacking images centered on the object coordinates. The degree to which the confusion noise is thereby reduced depends on the degree to which the (confusing) sources are randomly distributed with respect to the population of interest. In the case of deep 24μm observations, the clustering is relatively weak (i.e., most close pairs of galaxies are projections rather than physical associations) and the background is already largely resolved (i.e., more than 50% of the total extragalactic 24μm flux is in individually-detected sources; Dole et al. 2004; Papovich et al. 2004), making these data almost ideal for a stacking analysis. Hence, the combination of many images can substantially reduce the background noise and allow detection of the average flux of a given population, well below the canonical detection limit.

How well this works in practice and how best to stack, we explore with a number of tests. As is clear from Fig. 1, a substantial portion of 24 μm images have significant contributions from bright sources. In order to avoid that the "background" in stacked images is contaminated by small numbers of bright sources, we first identified and PSF-subtracted all sources that were individually detected above the 83 μJy level. The right-hand panel of Fig. 1 shows a residual image constructed in this way. We tested the efficacy of stacking these cleaned images in two ways. First, we measured the RMS of the background in a randomly placed 5″ aperture (the same aperture used for the galaxy photometry) as a function of number of images stacked. Postage stamp images with a size of $1'.68 \times 1'.68$ were randomly extracted from the residual image and stacked. We quantify the background noise by modified, outlier-resistant measure of the variance, defined as the half width of the range centered at the median value and including 68% of the sample values. Fig. 2 shows the decrease in σ_{bg} with increasing stack number: the effective background noise decreased as the inverse square root of the stack number. This behavior is as expected for ideal, uncorrelated random noise. The ideal behavior of the noise is a consequence of the flat number count spectrum at low flux levels at 24 μm, and it has the benefit that a standard error analysis is useful on the stacked images. Only below $\sigma_{bg} \sim 0.4$, which corresponds to a "5σ" limit of ~3 to 4 μJy, does the effective background noise become significantly larger than that predicted by the inverse square law extrapolation (see also Fig. 3). Second, we tested the accuracy of recovering artificial sources from image stacks, by randomly placing large numbers of individually faint, identical sources into the source subtracted image. Fig. 3 shows the results: stacking is able to recover progressively fainter signals with larger stack numbers. Roughly speaking, for data of this quality ($\sim$ 1380 seconds per pixel slow scan map in a low background field), a 35 μJy signal can be recovered in a ~10-image stack with a flux accuracy of ±50% at the 3σ detection level, and a 8 μJy signal can be recovered with a ~100-image stack. In our stacking, postage stamp images are aligned to a few tenths of one pixel. Alignment to the centroid pixel, i.e., to an accuracy of one pixel, causes an additional 5% error on the final recovered flux.

3.2. *Stacking of intermediate redshift galaxies*

To determine the characteristic thermal IR (24 μm) flux for sub-sets of galaxies to $z \sim 1$, a sample was drawn from the COMBO-17 redshift survey, where it overlaps with the MIPS 24 μm image. We divided the total sample of 7892 galaxies into 9 equally-spaced redshift slices from $0.1 \leq z < 1$ and within each redshift slice, into several rest-frame B-band luminosity bins, scaled at each redshift to the characteristic absolute magnitude (M_B^*) of the luminosity function derived by the VIMOS survey (Ilbert et al. 2005). Each luminosity bin covers one magnitude; adoption of a smaller magnitude bin would not change our results. We first illustrate which galaxies are individually detected through Fig. 4, which shows the rest-frame color $U - V$ of the sample galaxies versus the

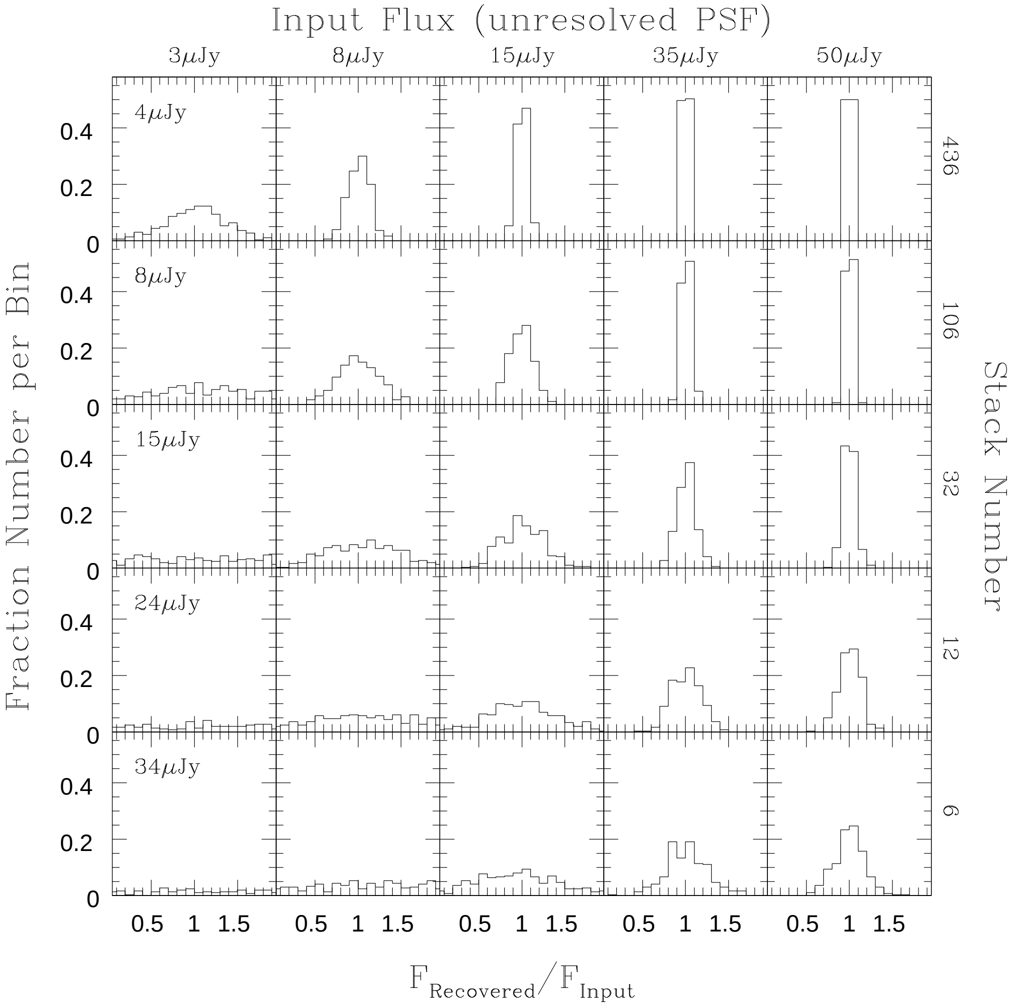

FIG. 3.— Recovery of simulated sources with different input flux levels as a function of stack number. The intervals between stack numbers are identical in logarithm space. Assuming Poisson noise, the expected "5σ" limits for corresponding stack numbers are given in the left hand panels. The detection limit $83\,\mu$Jy corresponds to stack number $N_{\rm stack} = 1$. As the simulated sources in one stack set are identical, median stack and mean stack give almost the same recovery. Here median stack values are adopted.

absolute B band magnitude. Open circles denote galaxies individually detected above $83\,\mu$Jy by MIPS; dots denote galaxies without individual detections. The dotted lines on the right-hand side of each panel show the value of M_B^* in each redshift bin, while the dotted line on the left-hand side denotes the faintest magnitude of galaxies stacked in this paper. In the two lowest redshift slices, $0.1 \leq z < 0.2$ and $0.2 \leq z < 0.3$, the objects at the faint end have an abnormal color distribution, and have an unusually high incidence of detections at $24\,\mu$m. Inspection of VVDS redshifts (Le Fevre et al. 2004) and GEMS morphologies (Rix et al. 2004) of galaxies in the low-luminosity, low-z bin argues strongly for a significant contamination by intrinsically more luminous galaxies at higher redshift. For very faint objects ($m_R \sim 23.5$ mag) with a featureless blue continuum, it is difficult to determine their redshift by either photometry or spectroscopy. Such objects are likely to be low-z blue dwarf galaxies or luminous star-forming galaxies at high-z ($>\sim 1.1$; where the 4000Å break is redshifted out of COMBO-17 broad I-band coverage). It is supported by the phenomenon that the high incidence of detections at $24\,\mu$m occurs only in the low-luminosity and low-z bins. Contamination by high-z objects to the low-z objects is difficult to quantify. Accordingly, we excluded these faint objects from our investigation. It is worth noting that owing to COMBO-17's R-band selection, the faintest bin of the sample becomes incomplete at all redshifts $z \gtrsim 0.6$; future work with a near IR-selected galaxy population can remedy this incompleteness.

For each bin in magnitude and redshift, $1'.68 \times 1'.68$ $24\,\mu$m postage stamps from the PSF-subtracted image centered on the positions of the individually-undetected objects (see Fig. 1) were cut out and then stacked. The size of the stamps is chosen to have sufficient area to properly estimate background. Two stacks were constructed for each sub-sample: a stack in which each pixel is the mean, or alternatively the median of all contributing pixels. The mean stack has the advantage that it includes the flux contributed from each galaxy, but has the disadvantage that it is more susceptible to residual flux from nearby sources. The median stack will underestimate the total flux somewhat, as the contributions from bright, nearly-detected sources will not be incor-

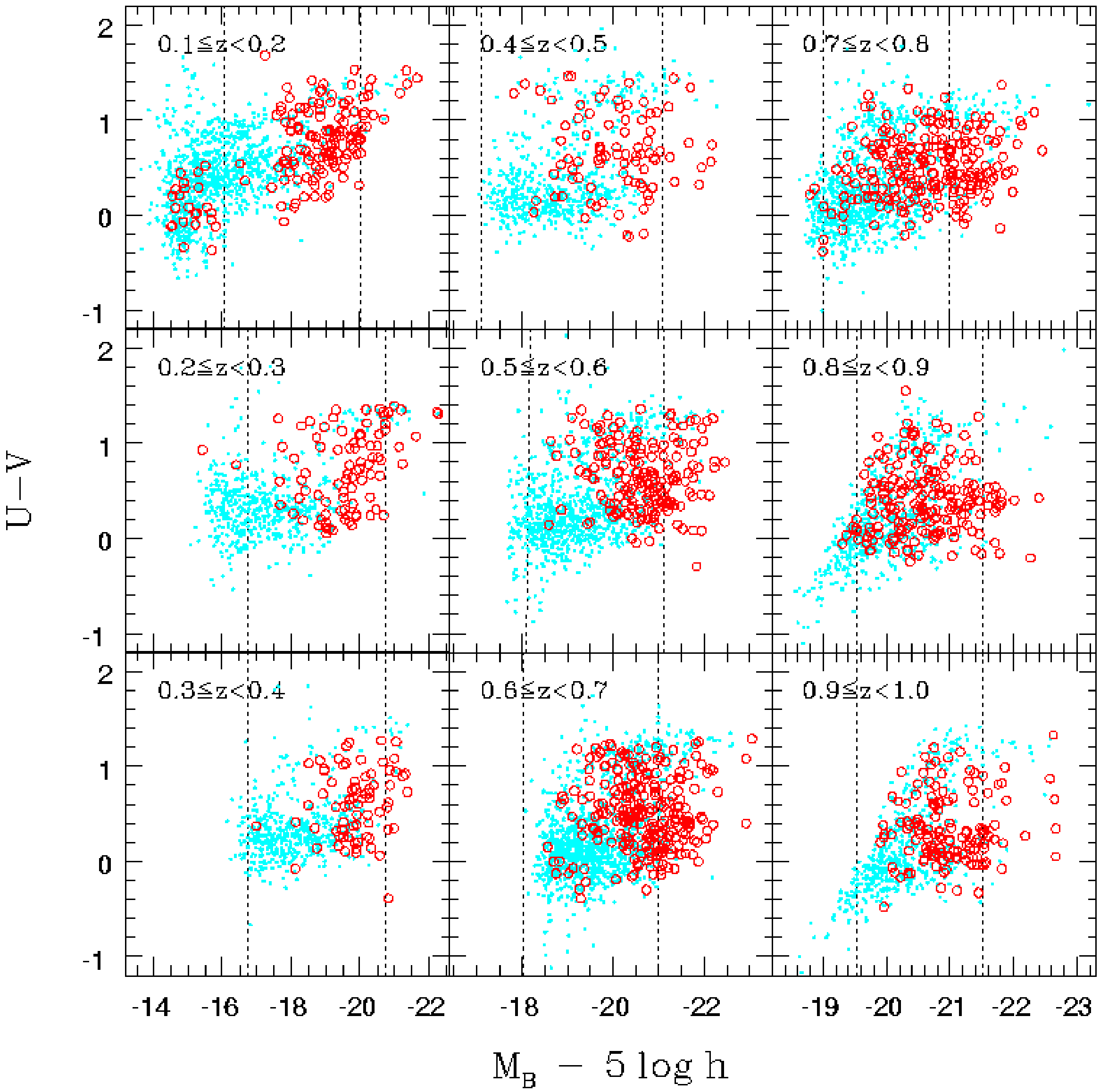

Fig. 4.— COMBO-17 galaxy sample in the CDFS: each panel shows the rest-frame color $U-V$ as a function of B band absolute magnitude for objects in 9 different redshift slices, increasing in redshift from top to bottom and left to right. In each panel, the right-hand side dotted line shows M^* and the dotted line on the left shows the limit of the faintest bin considered in this work. The M_B^* adopted from Ilbert et al. (2005) is -20.0, -20.7, -21.1, -21.0 and -21.5 for redshift bins $0.1 \leq z < 0.2$, $0.2 \leq z < 0.4$, $0.4 \leq z < 0.6$, $0.6 \leq z < 0.8$ and $0.8 \leq z < 1$, respectively. Sources individually detected at 24 μm are shown as open circles; undetected sources are denoted by dots. The population of very faint 24 μm individually-detected sources at $z \leq 0.3$ consists of much more luminous galaxies at high redshift which were mistakenly assigned COMBO-17 photometric redshifts $z \leq 0.3$ (see text for more discussion).

porated properly, but has the advantage that it is more robust to contamination from nearby sources. Furthermore, the background values for the mean stack will be contaminated by sources, whereas the median will be more robust. Therefore, in the following we adopt two measures of the stack flux: the integrated 5″ aperture flux of the median stack (using the median stack background value for sky subtraction), a lower limit to the flux; and, the integrated central flux within an aperture of radius 5″ of the mean-stacked image, using the background estimate from the median-stacked image as the background, giving an upper limit to the flux. Finally, the empirically-derived correction of a factor of 1.881 was used to aperture correct the estimates of stack flux to total. Fig. 5 shows 4 examples of median-stacked images. All median-stacked and mean-stacked images are electronically provided in Appendix. Stack fluxes and their uncertainties are listed in Table 1, along with total object numbers and stack numbers in each bin. Note that these mean flux estimates do not contain the flux contribution from the individual detections from each galaxy sub-sample.

4. RESULTS

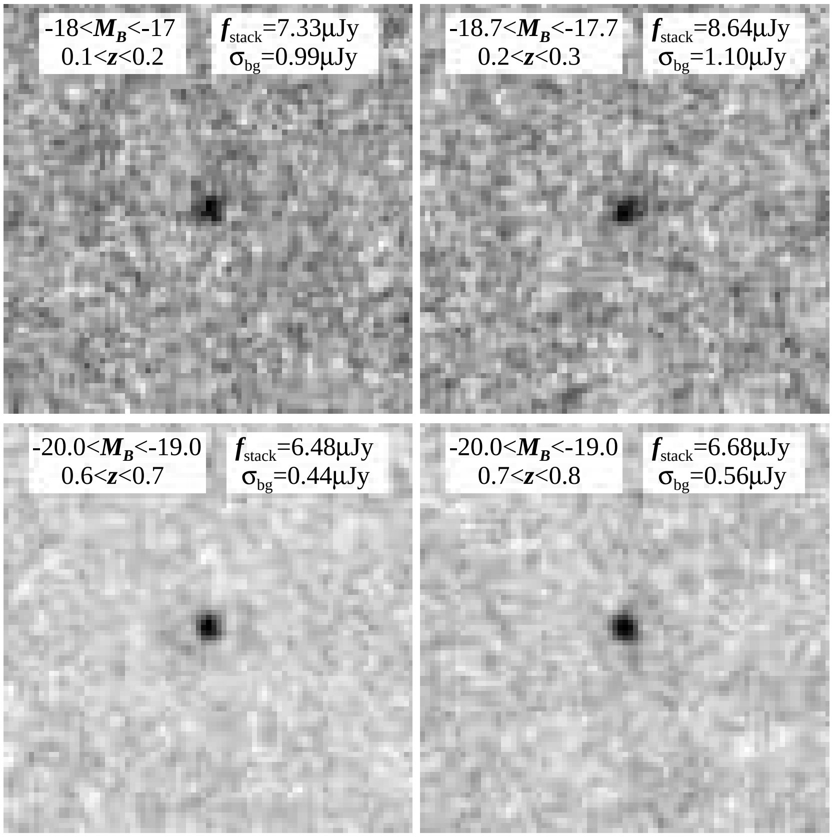

FIG. 5.— Examples of median-stacked 24 μm images. The magnitude bin, redshift slice, integrated flux of the central target within an aperture of radius $5''$, $f_{\rm stack}$ and background fluctuation $\sigma_{\rm bg}$ on the same aperture are labeled. Both $f_{\rm stack}$ and $\sigma_{\rm bg}$ are given in units of μJy. No aperture correction is implemented. The size of each image is $1'.68 \times 1'.68$. In bottom-left image, the second Airy ring of the 24 μm PSF is visible.

4.1. *Average SEDs and the contribution of individually-undetected sources*

Average luminosities at *rest-frame* 2800Å, Johnson U, B, and V-bands and at *observed-frame* 24 μm were calculated for each (redshift, luminosity) bin of galaxies. The 24 μm luminosity includes contributions from both individually-detected and individually-undetected sources. For the latter, the mean 24 μm intensity was estimated by stacking. Bootstrapping was used to estimate the uncertainty in total luminosity, i.e. randomly extracting the same number of sources from the parent set, either individually-detected sources or individually-undetected sources, then summing the luminosity from each subset. Table 2 lists average monochromatic luminosities (L_ν) in the rest-frame 2800 Å, standard Johnson U, B, V, and observed MIPS 24 μm bands for all magnitude bins in our investigation. Total UV luminosities derived from the UV2800 Å luminosities are given in unit of solar luminosity. Total IR luminosities and SFRs are also tabulated (see Sect. 4.2 & 4.3 for details). Fig. 6 shows the average 24 μm luminosities in different B-band magnitude bins over the redshift range $0.1 \leq z < 1$; luminosities in some of the optical bands (from Wolf et al. 2003) are shown to delineate the overall SED; the vertical errorbar is 1 "σ", which shows the 68% confidence region from bootstrapping. The horizonal bars show the band widths at each wavelength. Brighter galaxies in rest-frame B-band show higher mean 24 μm luminosities in all bands and redshifts than fainter galaxies. To place our measurements in context, three Spectral Energy Distribution (SED) templates from Devriendt et al. (1999) are arbitrarily scaled and shown alongside the observed SEDs. The three templates represent galaxies in three relevant modes of star formation: normal spiral galaxies, starbursts (M82) and massive starbursts (Arp 220). The importance of stacking in determining the average IR properties of distant galaxy populations can easily be discerned: the mean 24 μm fluxes of the faintest galaxies are an order of magnitude below the canonical "5σ" detection limit for individual detections for galaxies with $z \lesssim 0.7$, and are a factor of 5 below the individual detection limit for faint systems with $0.7 < z < 1$. Since the average 24 μm luminosity accounts for contributions from individually-detected sources, the mean 24 μm intensity of individually-undetected sources derived from stacking is indeed even lower.

Fig. 7 shows the 24 μm flux fractions derived from individual detections and from stacking. For the brightest galaxies ($M^* - 1 < M_B \leq M^*$), almost all of the flux arises from individual 24 μm detections across the redshift range $0.1 \leq z < 1$. The galaxies that are not individually detected have low average 24 μm luminosities; this is expected given that a substantial fraction of the most luminous galaxies in rest-frame B-band are "red sequence" galaxies which contain little recent star formation (Bell et al. 2004). For sub-L^* galaxies, the majority of galaxies in each bin are not detected individually.

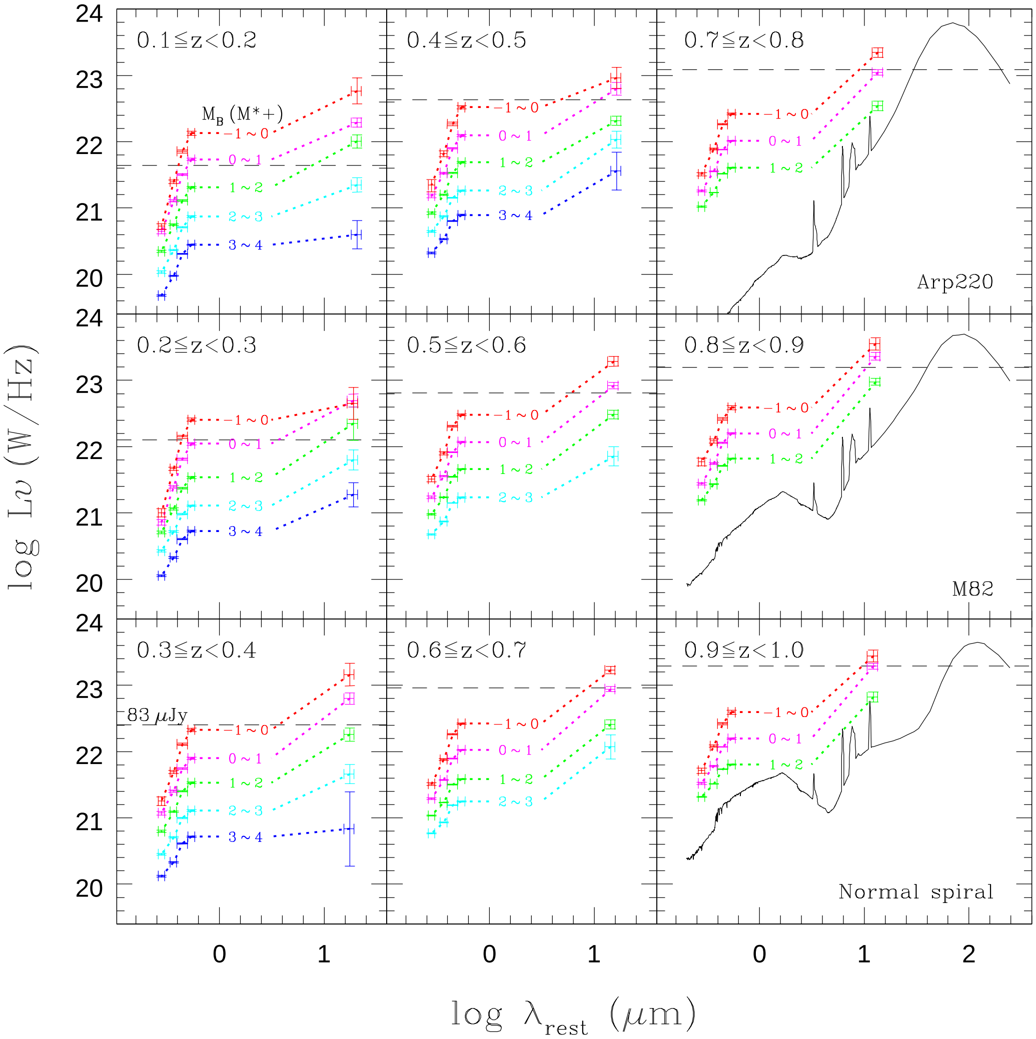

FIG. 6.— Average luminosities at rest-frame 2800Å, Johnson U, B, V-bands, and at observed-frame 24 μm for different magnitude bins (relative to an evolving M_B^*) and redshift slices. The label "−1 ∼ 0" refers to the magnitude bin $M^* - 1 < M_{\rm B} \leq M^* + 0$ and so forth. Three arbitrarily shifted SED templates are presented for comparison, taken from Devriendt et al. (1999). Horizontal dashed lines show the 83 μJy detection limit.

However, a large fraction of the total luminosity in each redshift and luminosity bin comes from the individually-undetected sources, especially for samples with $z > 0.4$. For the faintest bin in each redshift slice, the contribution from individually-detected sources is typically small.

COMBO-17 survey presents optically identified type I AGNs (Wolf et al. 2004). Such objects are not included in our sample. However, optically obscured type II AGNs are not eliminated from our sample. Type II AGNs could potentially contribute to 24 μm flux. To estimate the contamination from the type II AGNs, we cross-correlated our sample with the extended CDFS X-ray point source catalogs from 1 Ms CDFS and 250 ks *Chandra* observations (Lehmer et al. 2005). We identified 123 galaxies in our sample as X-ray detected type II AGNs. We found that the average 24 μm luminosities decrease approximately 5% for galaxies at $M_B < M^*{+}2$ by removing the 123 objects. Low luminosity galaxies are almost not affected. For X-ray undetected type II AGNs (to 250 ks exposure) with optical counterparts at m_R <24, radio and mid-IR investigations (Donley et al. 2005; Martínez-Sansigre et al. 2005) suggest that they are not more than X-ray detected ones. Then type II AGN's contribution to the average 24 μm luminosity is most likely up to ∼10% in our analysis. This effect is negligible compared with uncertainties in estimating average IR luminosities (typically ∼0.3 dex; see Table 2). On the other hand, it is still unclear whether IR emission in obscured AGNs is mostly related to AGN activity or star formation in their host galaxies. We conclude that obscured AGNs have insignificant effect on our conclusions.

4.2. *The relationship between IR/UV and rest-frame B-band luminosity*

Local star-forming galaxies exhibit a clear correlation between the $L_{\rm IR}/L_{\rm UV}$ ratio and rest-frame B-band luminosity (e.g. Wang & Heckman 1996; Bell 2003), in the

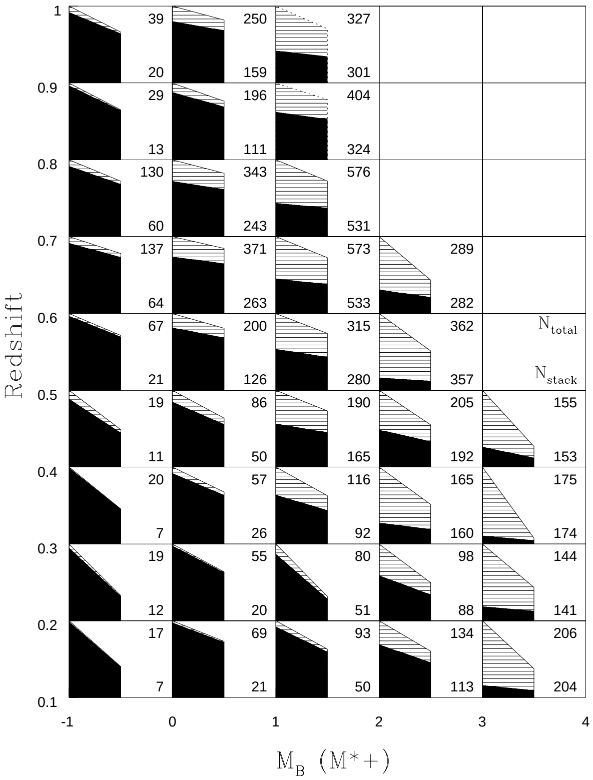

FIG. 7.— The relative contribution from individually-detected sources (heavily shaded region) at 24 μm compared to the contribution from undetected sources (lightly shaded region) for different magnitude bins in different redshift slices. In each panel, the left-hand side of shaded region shows the results for mean stacking scaled to unit and the right-hand side shows those for median stacking linearly normalized to mean-stack values, incorporating bootstrap error (the left-hand side shows the total mean-stack flux+1σ bootstrapping error, and the right-hand side shows the total median-stack flux−1σ); the heavily shaded region shows the contribution from individually-detected sources (from the left-hand side to the right-hand side, the height of heavily shaded region relative to overall shaded region shows minimal estimate of the contribution to maximal estimate). The total number of galaxies and number of individually-undetected galaxies stacked are shown in the upper and lower-right respectively. Dotted lines denote those magnitude bins having bias against red galaxies due to the R-band selection effect.

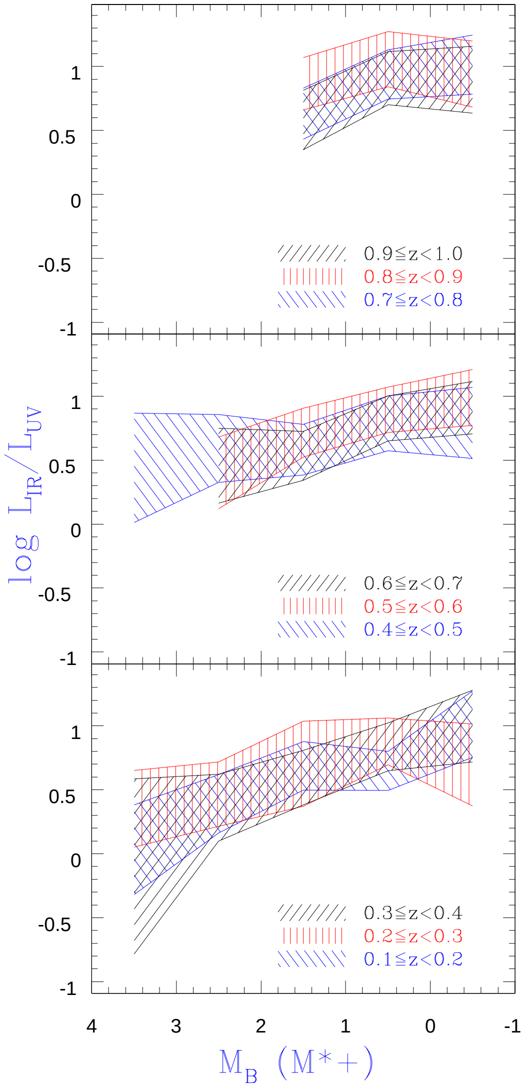

FIG. 8.— Relationship between the mean $L_{\rm IR}/L_{\rm UV}$ ratio and rest-frame B-band luminosity, scaled to M^*_B, covering $0.1 \leq z < 1$. The $L_{\rm IR}/L_{\rm UV}$ ratio increases with luminosity, i.e., brighter objects show a higher $L_{\rm IR}/L_{\rm UV}$ ratio.

sense that lower-luminosity galaxies typically possess a lower $L_{\rm IR}/L_{\rm UV}$ ratio albeit with large scatter. While we cannot test the validity of this relation galaxy-by-galaxy at intermediate redshift using the current datasets, we can investigate its validity of this relation in an average sense using stacking.

Fig. 8 shows the $L_{\rm IR}/L_{\rm UV}$ ratio as a function of rest-frame B-band luminosity at $0.1 \leq z < 1$. COMBO-17's observed-frame R-band selection allows access to galaxies as faint as $0.04\,L^*$ (i.e., $M^* + 3.5$) up to $z \sim 0.45$, $0.1\,L^*$ (i.e., $M^* + 2.5$) up to $z \sim 0.65$, and $0.25\,L^*$ (i.e., $M^* + 1.5$) up to $z \sim 0.95$. Owing to Spitzer's lower sensitivity and larger PSF at wavelengths beyond 24 μm, the vast majority of galaxies are undetected at longer wavelengths. Therefore the total IR flux must be estimated from the 24 μm flux by a rather large extrapolation, using suites of local templates[7]. Several sets of luminosity-dependent templates are used to estimate the total IR luminosity over $\lambda_{\rm rest} = 8 - 1000\,\mu$m and its uncertainty (See Le Floc'h et al. 2005 for more details and an extensive discussion of observational tests of 24 μm-to-total-IR corrections; see also Chary & Elbaz 2001, Papovich & Bell 2002 and Dale et al. 2005 for more discussions). In Fig. 8 the shaded region shows the lower and upper limits for the $L_{\rm IR}/L_{\rm UV}$ ratio mainly due to the uncertainty of $L_{\rm IR}$. Here the lower limit refers to median-stack total flux $- 1\sigma$ bootstrapping error $- 1\sigma$ IR luminosity error and the upper limit to mean-stack total flux $+ 1\sigma$ bootstrapping error $+ 1\sigma$ IR luminosity error. The $L_{\rm IR}/L_{\rm UV}$ ratio is correlated with rest-frame B-band luminosity at all redshifts up to at least $z \sim 0.8$. Brighter galaxies on average show a higher $L_{\rm IR}/L_{\rm UV}$ ratio, consistent with the sense of the local relation. As COMBO-17's observed-frame R-band selection may exclude red galaxies in the

---

[7] We will tackle the technically-challenging stacking of longer-wavelength Spitzer data in an upcoming work.

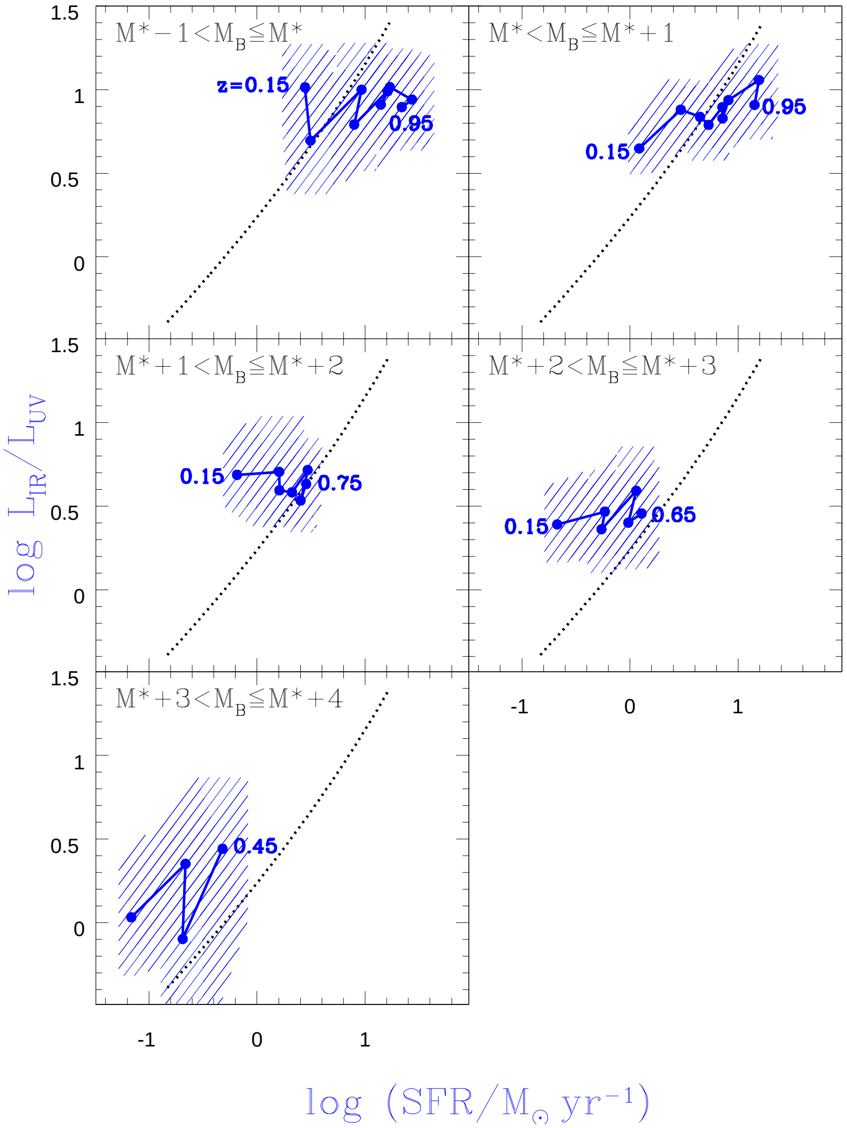

FIG. 9.— The mean $L_{\rm IR}/L_{\rm UV}$ ratio as a function of SFR for galaxies in magnitude bins from $M^* - 1 < M_B \leq M^*$ to $M^* + 3 < M_B \leq M^* + 4$. The heavy lines show increasing redshift, from left to right, with the minimum and maximum values of z at the corresponding ends of the lines. The local relation, recently re-derived using GALEX and IRAS data, is shown with dotted lines (Martin et al. 2005).

faintest bin at $z \gtrsim 0.6$, it is conceivable in these cases that the $L_{\rm IR}/L_{\rm UV}$ ratio is underestimated (and especially at $z \gtrsim 0.8$) due to a deficiency of red galaxies.

4.3. *The relationship between $L_{\rm IR}/L_{\rm UV}$ and SFR at $z < 1$*

Hopkins et al. (2001) and Adelberger & Steidel (2000) explore the relationship between UV-extinction and SFR, arguing for a universal correlation between extinction and SFR. In this section, we explore this issue using our stacked dataset.

For the data at hand, we estimate the SFR from a combination of UV (the directly-observed emission from young stars) and IR luminosities (dominated by reprocessed UV light from young stars; e.g., Gordon et al. 2000). The IR luminosity in turn is estimated from the 24 μm luminosity. Following Bell et al. (2005), we estimate the "total" UV luminosity, from 1216 Å to 3000 Å, from COMBO-17's 2800Å monochromatic luminosity using $L_{UV} = 1.5\,\nu L_{\nu,2800}$. This conversion assumes a stellar population with a constant SFR for 100 Myr and a Kroupa IMF. The same stellar population is then used to calibrate the total SFR:

$$\mathrm{SFR}/(M_\odot\,\mathrm{yr}^{-1}) = 9.8 \times 10^{-11} \times (L_{\rm IR} + 2.2\,L_{\rm UV}), \quad (1)$$

where $L_{\rm IR}$ is the total IR luminosity in units of solar luminosity (see Bell et al. 2005 for further description of the assumptions behind this SFR calibration).

Fig. 9 shows the $L_{\rm IR}/L_{\rm UV}$ ratio as a function of SFR split into 5 bins of optical luminosity. The local relationship, recently re-derived by Martin et al. (2005) using GALEX and IRAS data, is also shown[8]. From the nearby universe back to $z \sim 1$, both $L_{\rm IR}/L_{\rm UV}$ and SFR increase at a given optical luminosity relative to L^*_B. At all redshifts and luminosities, galaxies follow approximately the local trend for $L_{\rm IR}/L_{\rm UV}$ and SFR to within the (considerable) uncertainties. In particular, as one considers fainter and fainter optical luminosity (from comparison of the different panels), galaxies have lower SFRs and $L_{\rm IR}/L_{\rm UV}$ values, again in agreement with locally-observed galaxies. Thus, to within the systematic uncertainties, we see no evidence against the proposition that $0.1 < z < 0.8$ star-forming galaxies obey on average the local $L_{\rm IR}/L_{\rm UV}$–SFR correlation. Beyond $z \sim 0.8$, the incompleteness of the sample makes such inferences inconclusive. This relationship has been studied on a galaxy-by-galaxy basis at $z \sim 0.7$ by Bell et al. (2005) for individually-detected IR-luminous galaxies. These distant star-forming galaxies were found to approximately follow the local $L_{\rm IR}/L_{\rm UV}$–SFR correlation, again to within the considerable uncertainties and with very large (> 0.5 dex) scatter. We stress that such scatter invalidates attempts at implementing the relationship to individual very luminous infrared galaxies with SFR $>20\,{\rm M}_\odot\,{\rm yr}^{-1}$.

---

[8] Martin et al. derive UV luminosities using νl_ν at 1500Å, which

5. COSMIC IR LUMINOSITY DENSITY

The cosmic IR luminosity density is essential to estimate of the cosmic star formation rate (e.g., Le Floc'h et al. 2005). It can be derived from the infrared luminosity function. Due to limited detection depth in the infrared, the faint end slope of the infrared luminosity function is poorly constrained, resulting in large uncertainty in estimating the cosmic IR luminosity density (Pérez-González et al. 2005). Our stacked dataset probes flux levels below the individually-resolved flux in deep 24 μm images. Hence, our results can provide new constraints on the cosmic IR luminosity density, which can be then used to constrain the slope of the faint end of the infrared luminosity function.

We derived average IR luminosity for galaxies of known rest-frame B-band luminosity. By Comparing with B-band luminosity function, we are able to estimate the total infrared luminosity density. Similar to Fig. 8, we show the relation between $L_{\rm IR}/\nu L_{\nu,{\rm B}}$ ratio and the $B-$band magnitude in Fig. 10. We fitted the behavior in this figure and used the fits to extrapolate to fainter luminosities. The fits are given by the equations

$$\log\, L_{\rm IR}/\nu L_{\nu,{\rm B}} = -0.14 \times M_{\rm B} + (0.6 \pm 0.3) \tag{2}$$

and

$$\log\, L_{\rm IR}/\nu L_{\nu,{\rm B}} = -0.03 \times M_{\rm B} + (0.5 \pm 0.3) \tag{3}$$

for 0.1≤ z <0.4 and 0.4≤ z <0.7, respectively. Here the B-band magnitude is scaled to $M^*_{\rm B}$. For redshift bins 0.7≤ z <1, we adopted the same slope as found for 0.4≤ z <0.7 but left the normalization free, to derive:

$$\log\, L_{\rm IR}/\nu L_{\nu,{\rm B}} = -0.03 \times M_{\rm B} + (0.8 \pm 0.3). \tag{4}$$

The fits indicate that galaxies at the faint end are similar to bright ones in the $L_{\rm IR}/\nu L_{\nu,{\rm B}}$ ratio, consistent with the finding of no correlation between the $L_{\rm IR}/\nu L_{\nu,{\rm B}}$ ratio and B-band luminosity by Wang & Heckman (1996).

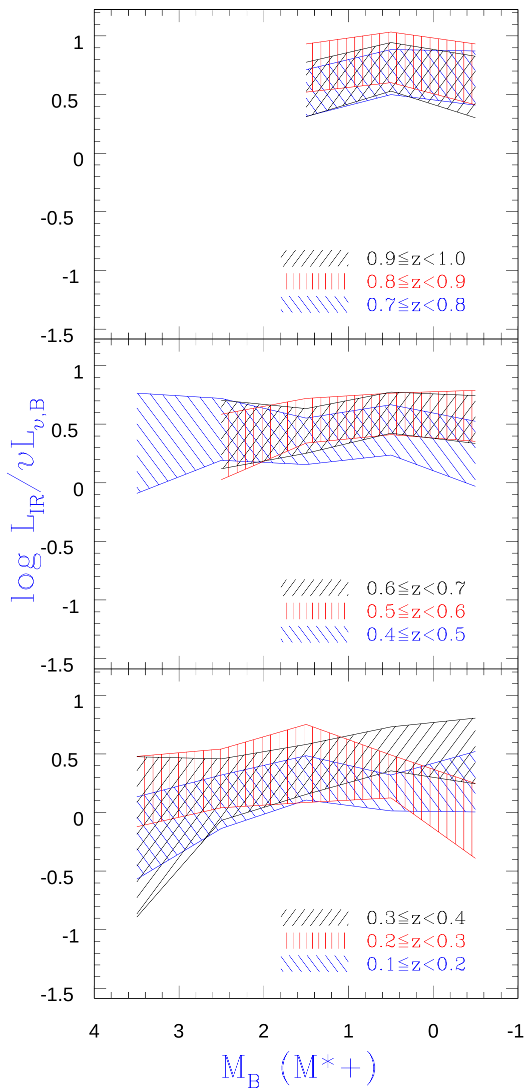

FIG. 10.— The relationship between mean $L_{\rm IR}/L_{\rm B}$ ratio and rest-frame B-band luminosity, scaled to M^*_B, covering $0.1 \leq z < 1$. The $L_{\rm IR}/L_{\rm B}$ ratio is roughly independent of luminosity to first order.

Together with the rest-frame B-band luminosity function of Ilbert et al. (2005), we calculated the total IR luminosity density. In Fig. 11 we show the total IR luminosity density as a function of redshift. Due to the observed-frame R-band selection, an increasing fraction of the total IR luminosity comes from the extrapolated part of the LF with increasing redshift. Since the B-band luminosity function is well determined in several deep redshift surveys (e.g. Faber et al. 2005), our results should not underestimate the cosmic infrared luminosity density. Similar results were obtained with the B-band luminosity function of the DEEP2 survey (Willmer et al. 2005). Fig. 11 exhibits that the cosmic luminosity density increases by a factor of 9±3 from $z = 0.1$ to $z = 1$.

We compare our result with the total IR luminosity density given by the infrared luminosity function of Le Floc'h et al. (2005) in Fig. 11. The two estimates of the total IR luminosity density are identical to within the errors over the redshift range 0.1≤ z <1. This is

---

yields values comparable to our definition of total UV for constant SFR populations. That work uses $L_{\rm IR} = (\nu L_\nu)_{60\,\mu{\rm m}}$; these values are roughly a factor of two lower than our definition of IR luminosity (see, e.g., Bell 2003). We account for these differences in definition when comparing with the Martin et al. relation.

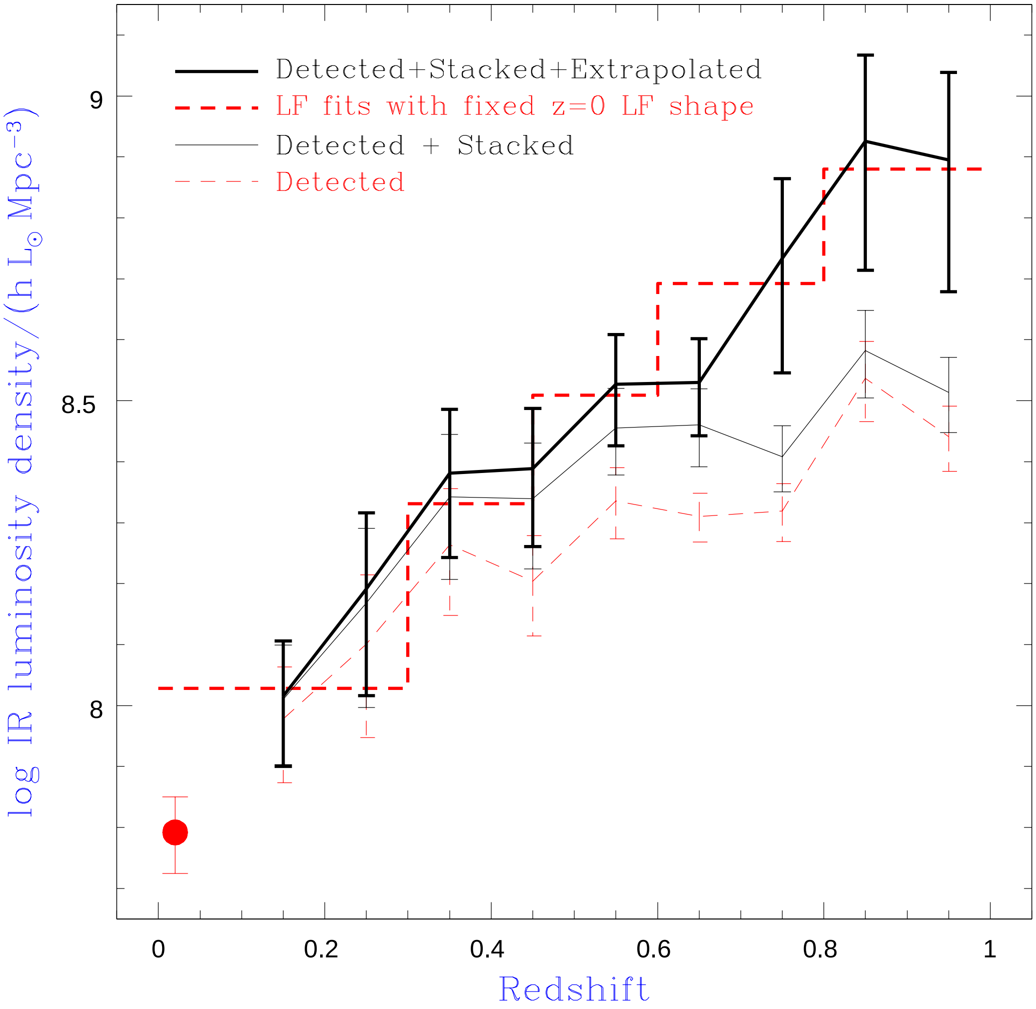

Fig. 11.— IR luminosity density as a function of redshift. The thin solid line is the IR luminosity density attributed to galaxies whose population-averaged $L_{\rm IR}/L_{\rm B}$ ratio is known from Fig. 10. By extrapolating the relation between $L_{\rm IR}/L_{\rm B}$ and $L_{\rm B}$ to the faint end, the total IR luminosity density derived from the B-band luminosity function is obtained and shown as the thick solid line. The thin dashed line shows the contribution from galaxies individually detected at 24 μm ($> 83\,\mu$Jy). The thick dashed line shows the IR luminosity density given by the infrared luminosity function (Le Floc'h et al. 2005). The dot shows the local IR luminosity density (Takeuchi et al. 2003). The thick dashed line and thick solid line are well matched.

important, as both estimates were derived in very different ways. Le Floc'h et al. fit the evolving infrared luminosity function of individually-detected galaxies using the same functional form as determined in the local Universe, incorporating luminosity and density evolution. In contrast, we directly detect the average flux of faint galaxies not individually detected by MIPS, and then use the trend in $L_{\rm IR}/L_{\rm B}$ as a function of $L_{\rm B}$ to estimate the IR luminosity residing in galaxies faintwards of our optical completeness limit (it should be noted that the shape of the optical luminosity function to deeper limits has been tested directly by the VVDS and e.g., in the HDF N and S, thus our extrapolation could be considered to be relatively well-posed). This comparison would tend to support Le Floc'h et al.'s claim that the faint end slope of IR luminosity function is unlikely to be very steep. We have tested this directly by re-fitting the IR luminosity functions of Le Floc'h et al. (2005), using our estimated total IR luminosity (with our derived error bars) as a constraint. Such an analysis gives a power law slope of 1.2±0.3 (to be compared to the local value of 1.23; Takeuchi et al. 2003; see also Pérez-González et al. 2005 for a power law index of 1 to 1.3 up to $z = 1$ and beyond).

6. DISCUSSION AND CONCLUSION

Estimating the importance of dust-obscured star formation for intermediate-redshift normal, or even low-luminosity galaxies on a galaxy-by-galaxy basis is impossible through direct thermal IR observations with current technology. Using 24 μm images from Spitzer, we show that one can determine mean thermal IR fluxes and hence 10-fold fainter average obscured star formation rates by stacking 24 μm images centered on the optical positions of known intermediate-redshift galaxies. We use a sample of galaxies from the COMBO-17 photometric redshift survey of the Extended Chandra Deep Field South, which provides astrometry, photometric redshift and rest-frame 2800Å, U, B, and V-band absolute magnitudes for thousands of $z \lesssim 1$ galaxies. We stack MIPS $24\,\mu$m images for subsamples of galaxies in redshift slices and rest-frame B-band luminosity bins, allowing detection of average $24\,\mu$m fluxes down to $< 10\,\mu$Jy, an order of magnitude deeper than those accessible on a galaxy-by-galaxy basis.

The mean total IR luminosity of these galaxy subsets is estimated from the observed $24\,\mu$m luminosity, taking into account the uncertainty of IR SED shapes. Analogous mean UV luminosities are derived, and average SFRs are estimated from the UV and IR luminosities of each subsample. We use these data to examine the correlations among optical luminosity, dust obscuration, SFR and redshift.

We find that the correlation between dust obscuration, i.e. the ratio of $L_{\rm IR}/L_{\rm UV}$, and rest-frame B-band luminosity seen in local star-forming galaxies holds over all redshifts $z \lesssim 1$, with brighter galaxies showing a higher $L_{\rm IR}/L_{\rm UV}$ ratio. Our averaged $24\,\mu$m detections show directly that even in low luminosity galaxies (to $0.05\,L^*$) the majority of the bolometric luminosity from young stars is re-radiated in the thermal IR. Nonetheless, the decrease of $L_{\rm IR}/L_{\rm UV}$ ratio with decreasing $L_{\rm B}$ implies that globally star formation in faint objects is lower than the estimate one would derive the level of dust obscuration typical of normal galaxies.

We explore the correlation between average $L_{\rm IR}/L_{\rm UV}$ ratios and SFRs for the different optically-selected subsamples. Different subsamples populate different parts of the $L_{\rm IR}/L_{\rm UV}$–SFR plane; however, our data indicate that this correlation does not evolve much between $z = 1$ and the present day.

In closing, we briefly consider some of the factors determining the degree of dust obscuration indicated by $L_{\rm IR}/L_{\rm UV}$ and roughly parameterized as an optical depth, τ. The optical depth of a galaxy $\tau \propto \Sigma_{\rm gas}\, Z\, \alpha$, where $\Sigma_{\rm gas}$ is gas density, Z is metallicity and α is a geometric term to account for the gas and dust distribution relative to massive stars. Star formation intensity is strongly correlated with gas density, e.g., the Schmidt law (Kennicutt 1998b). Since our results are drawn from a large number of galaxies, geometric effects may cancel out, to first order. Then the correlation of $L_{\rm IR}/L_{\rm UV}$, or τ with SFR (i.e., more intense star-forming environments show larger dust obscuration) may suggest that gas density drives $L_{\rm IR}/L_{\rm UV}$ correlation to a much greater extent than Z, at least over the magnitude and redshift ranges we consider in this work.

Independent from the infrared luminosity function, we estimate the cosmic infrared luminosity density from the rest-frame B-band luminosity function. An increase by a factor of $9{\pm}3$ is found for the comoving infrared luminosity density from $z = 0.1$ to $z = 1$, consistent with Le Floc'h et al. (2005). Based on our estimate of the comic infrared luminosity density, it is suggested that the infrared luminosity function of Le Floc'h et al. (2005) is well determined at intermediate redshifts, supporting their claim that faint end slope of the luminosity function is relatively flat. Our result suggests a power law index of 1.2 ± 0.3.

We thank John Peacock for helpful discussions. We thank the referee for helpful comments, which improved this manuscript. Support for this work was provided by NASA through contract number 960785 issued by JPL/Caltech. E. F. B. was supported by the European Community's Human Potential Program under contract HPRN-CT-2002-00316, SISCO. This publication made use of NASA's Astrophysics Data System Bibliographic Services.

REFERENCES

Adelberger, K. L., & Steidel, C. C. 2000, ApJ, 544, 218
Bauer, A. E., Drory, N., Hill, G. J., & Feulner, G. 2005, ApJ, 621, L89
Bell, E. F. 2003, ApJ, 586, 794
Bell, E. F., et al. 2004, ApJ, 608, 752
Bell, E. F., et al. 2005, ApJ, 625, 23
Bertin, E., & Arnouts, S. 1996, A&AS, 117, 393
Brinchmann, J., & Ellis, R. S. 2000, ApJ, 536, L77
Buat, V., et al. 2005, ApJ, 619, L51
Bundy, K., Ellis, R. S., & Conselice, C. J. 2005, ApJ, 625, 621
Calzetti, D., & Heckman, T. M. 1999, ApJ, 519, 27
Chary, R., & Elbaz, D. 2001, ApJ, 556, 562
Dale, D. A., et al. 2005, ApJ, in press (astro-ph/0507645)
Devriendt, J. E. G., Guiderdoni, B., & Sadat, R. 1999, A&A, 350, 381
Dole, H., et al. 2004, ApJS, 154, 93
Donley, J. L., Rieke, G. H., Rigby, J. R., Pérez-González P. G. 2005, ApJ in press (astro-ph/0507676)
Faber, S. M., et al. 2005, ApJ, submitted (astro-ph/0506044)
Franceschini, A., et al. 2003, A&A, 403, 501
Gordon, K. D., Clayton, G. C., Witt, A. N., & Misselt, K. A. 2000, ApJ, 533, 236
Gordon, K. D., et al. 2005, PASP, 117, 503
Heavens, A., Panter, B., Jimenez, R., & Dunlop, J. 2004, Nature, 428, 625
Hopkins, A. M. 2004, ApJ, 615, 221
Hopkins, A. M., Connolly, A. J., Haarsma, D. B., & Cram, L. E. 2001, AJ, 122, 288
Ilbert, O., et al. 2005, A&A, in press (astro-ph/0409134)
Juneau, S., et al. 2005, ApJ, 619, L135
Kennicutt, Jr., R. C. 1998a, ARA&A, 36, 189
Kennicutt, Jr., R. C. 1998b, ApJ, 498, 541
Le Févre, O., et al. 2004, A&A, 428, 1043
Le Floc'h E., et al. 2005, ApJ, 632, 169
Lehmer, B. D., et al. 2005, ApJS, 161, 21
Madau, P., Ferguson, H. C., Dickinson, M. E., Giavalisco, M., Steidel, C. C., & Fruchter, A. 1996, MNRAS, 283, 1388
Martin, D. C., et al. 2005, ApJL, 619, L59
Martínez-Sansigre, A., et al. 2005, Nature, 436, 666
Meurer, G. R., Heckman, T. M., & Calzetti, D. 1999, ApJ, 521, 64
Mushotzky, R. F., & Loewenstein, M. 1997, ApJ, 481, L63
Papovich, C., & Bell, E. F. 2002, ApJ, 579, L1
Papovich, C., et al. 2004, ApJS, 154, 70
Pérez-González, P. G., et al. 2005, ApJ, 630, 82
Rieke, G. H., et al. 2004, ApJS, 154, 25
Rix, H.-W., et al. 2004, ApJS, 152, 163
Schiminovich, D., et al. 2005, ApJ, 619, L47
Steidel, C. C., Adelberger, K. L., Giavalisco, M., Dickinson, M., & Pettini, M. 1999, ApJ, 519, 1
Sullivan, M., Treyer, M. A., Ellis, R. S., Bridges, T. J., Milliard, B., & Donas, J. 2000, MNRAS, 312, 442
Takeuchi, T., Yoshikawa, K., & Ishii, T. T. 2003, ApJ, 587, L39
Wang, B., & Heckman, T. M. 1996, ApJ, 457, 645
Willmer, C. et al. 2005, ApJ, submitted (astro-ph/0506041)
Wolf, C., Meisenheimer, K., Rix, H.-W., Borch, A., Dye, S., & Kleinheinrich, M. 2003, A&A, 401, 73
Wolf, C., et al. 2004, A&A, 421, 913
Wolf, C., et al. 2005, ApJ, 630, 771
Zheng, X. Z., Hammer, F., Flores, H., Assémat, F., & Pelat, D. 2004, A&A, 421, 847

TABLE 1
TOTAL OBJECT NUMBERS, STACK OBJECT NUMBERS, 24μM STACK FLUXES AND BACKGROUND RMS FOR 37 SUBSAMPLES DEFINED BY REDSHIFT AND LUMINOSITY.

				Median-stack		Mean-stack	
z	$< M_B >$	N_{total}	N_{stack}	f_{stack}[a] (Jy)	σ_{bg}[a] (Jy)	f_{stack}[a] (Jy)	σ_{bg}[a] (Jy)
0.15	−16.5	206	204	3.37	0.76	2.82	0.87
	−17.5	134	113	7.33	0.99	7.13	1.08
	−18.5	93	50	11.90	1.59	12.82	1.69
	−19.5	69	21	12.00	2.02	14.26	2.72
	−20.5	17	7	22.80	3.65	18.73	3.82
0.25	−17.2	144	141	4.92	0.97	5.30	1.02
	−18.2	98	88	8.64	1.10	9.41	1.31
	−19.2	80	51	15.86	1.37	16.83	1.76
	−20.2	55	20	8.56	1.89	8.91	1.99
	−21.2	19	12	10.91	3.22	11.70	3.42
0.35	−17.2	175	174	1.02	0.82	0.77	0.96
	−18.2	165	160	5.47	0.90	5.37	0.98
	−19.2	116	92	12.89	1.05	13.49	1.05
	−20.2	57	26	17.42	2.02	17.03	2.23
	−21.2	20	7	6.34	3.92	4.55	3.95
0.45	−17.6	155	153	2.65	0.79	2.48	0.73
	−18.6	205	192	5.00	0.68	5.34	0.80
	−19.6	190	165	9.90	0.75	9.55	0.83
	−20.6	86	50	15.56	1.39	15.32	1.34
	−21.6	19	11	16.90	2.71	16.93	3.44
0.55	−18.6	362	357	3.71	0.48	3.69	0.61
	−19.6	315	280	10.02	0.54	9.85	0.59
	−20.6	200	126	14.53	0.95	15.37	1.04
	−21.6	67	21	12.20	1.96	11.78	1.99
0.65	−18.5	289	282	3.20	0.67	3.61	0.77
	−19.5	573	533	6.48	0.44	6.54	0.50
	−20.5	371	263	14.55	0.65	14.46	0.66
	−21.5	137	64	11.98	1.27	13.24	1.29
0.75	−19.5	576	531	6.68	0.56	6.98	0.54
	−20.5	343	243	14.78	0.67	14.80	0.77
	−21.5	130	60	10.94	1.39	12.52	1.60
0.85	−20.0	404	324	10.97	0.53	11.83	0.61
	−21.0	196	111	12.06	0.92	12.40	1.02
	−22.0	29	13	5.00	2.38	4.61	2.55
0.95	−20.0	327	301	8.44	0.62	8.74	0.76
	−21.0	250	159	12.25	0.86	12.22	1.00
	−22.0	39	20	6.49	2.67	6.75	2.75

[a] Within an aperture of radius 5″.

TABLE 2

AVERAGE LUMINOSITIES AND SFRS FOR GALAXY SUBPOPULATIONS OF GIVEN MAGNITUDE BINS OVER THE REDSHIFT RANGE $0.1 \leq z < 1$.

								Minimum[a]		Maximum[b]	
z	$< M_B >$	$\log L_{2800\AA}$ (W/Hz)	$\log L_{\rm U}$ (W/Hz)	$\log L_{\rm B}$ (W/Hz)	$\log L_{\rm V}$ (W/Hz)	$\log L_{24\mu{\rm m,obs}}$ (W/Hz)	$\log L_{\rm UV}$ ($L_\odot$)	$\log L_{\rm IR}$ ($L_\odot$)	$\log {\rm SFR}$ ($M_\odot\,{\rm yr}^{-1}$)	$\log L_{\rm IR}$ ($L_\odot$)	$\log {\rm SFR}$ ($M_\odot\,{\rm yr}^{-1}$)
0.15	-16.5	$19.681^{+0.012}_{-0.013}$	$19.977^{+0.009}_{-0.009}$	$20.308^{+0.008}_{-0.008}$	$20.448^{+0.009}_{-0.009}$	$20.65^{+0.16}_{-0.26}$	$8.30^{+0.01}_{-0.01}$	$8.17^{+0.13}_{-0.19}$	$-1.24^{+0.04}_{-0.04}$	$8.56^{+0.12}_{-0.17}$	$-1.10^{+0.06}_{-0.07}$
	-17.5	$20.033^{+0.018}_{-0.019}$	$20.367^{+0.012}_{-0.012}$	$20.710^{+0.011}_{-0.011}$	$20.874^{+0.013}_{-0.013}$	$21.36^{+0.10}_{-0.12}$	$8.65^{+0.02}_{-0.02}$	$8.96^{+0.11}_{-0.15}$	$-0.73^{+0.06}_{-0.07}$	$9.17^{+0.10}_{-0.14}$	$-0.62^{+0.06}_{-0.08}$
	-18.5	$20.347^{+0.019}_{-0.020}$	$20.747^{+0.013}_{-0.013}$	$21.115^{+0.012}_{-0.013}$	$21.315^{+0.015}_{-0.016}$	$22.02^{+0.09}_{-0.11}$	$8.97^{+0.02}_{-0.02}$	$9.58^{+0.09}_{-0.12}$	$-0.24^{+0.06}_{-0.07}$	$9.76^{+0.09}_{-0.11}$	$-0.12^{+0.06}_{-0.08}$
	-19.5	$20.646^{+0.030}_{-0.032}$	$21.110^{+0.017}_{-0.018}$	$21.506^{+0.014}_{-0.015}$	$21.734^{+0.017}_{-0.018}$	$22.29^{+0.06}_{-0.07}$	$9.27^{+0.03}_{-0.03}$	$9.86^{+0.08}_{-0.10}$	$0.05^{+0.05}_{-0.06}$	$9.99^{+0.08}_{-0.10}$	$0.13^{+0.06}_{-0.07}$
	-20.5	$20.725^{+0.039}_{-0.043}$	$21.395^{+0.025}_{-0.027}$	$21.854^{+0.025}_{-0.026}$	$22.128^{+0.028}_{-0.030}$	$22.81^{+0.15}_{-0.24}$	$9.34^{+0.04}_{-0.04}$	$10.19^{+0.07}_{-0.09}$	$0.30^{+0.05}_{-0.07}$	$10.54^{+0.07}_{-0.09}$	$0.59^{+0.06}_{-0.08}$
0.25	-17.2	$20.054^{+0.015}_{-0.016}$	$20.330^{+0.012}_{-0.012}$	$20.605^{+0.010}_{-0.010}$	$20.728^{+0.012}_{-0.012}$	$21.31^{+0.14}_{-0.22}$	$8.67^{+0.02}_{-0.02}$	$8.87^{+0.11}_{-0.15}$	$-0.76^{+0.05}_{-0.06}$	$9.22^{+0.11}_{-0.14}$	$-0.58^{+0.07}_{-0.08}$
	-18.2	$20.429^{+0.017}_{-0.018}$	$20.723^{+0.013}_{-0.014}$	$20.982^{+0.011}_{-0.011}$	$21.109^{+0.012}_{-0.012}$	$21.83^{+0.13}_{-0.18}$	$9.05^{+0.02}_{-0.02}$	$9.40^{+0.10}_{-0.14}$	$-0.31^{+0.05}_{-0.06}$	$9.67^{+0.09}_{-0.12}$	$-0.15^{+0.06}_{-0.08}$
	-19.2	$20.706^{+0.022}_{-0.023}$	$21.061^{+0.015}_{-0.015}$	$21.371^{+0.013}_{-0.014}$	$21.537^{+0.018}_{-0.019}$	$22.42^{+0.18}_{-0.32}$	$9.33^{+0.02}_{-0.02}$	$9.81^{+0.09}_{-0.12}$	$0.04^{+0.05}_{-0.07}$	$10.28^{+0.08}_{-0.10}$	$0.37^{+0.07}_{-0.08}$
	-20.2	$20.862^{+0.040}_{-0.045}$	$21.394^{+0.018}_{-0.019}$	$21.812^{+0.017}_{-0.018}$	$22.044^{+0.020}_{-0.021}$	$22.71^{+0.09}_{-0.11}$	$9.48^{+0.04}_{-0.04}$	$10.28^{+0.08}_{-0.10}$	$0.40^{+0.06}_{-0.07}$	$10.46^{+0.08}_{-0.10}$	$0.54^{+0.07}_{-0.08}$
	-21.2	$21.005^{+0.057}_{-0.066}$	$21.667^{+0.025}_{-0.027}$	$22.149^{+0.022}_{-0.023}$	$22.407^{+0.023}_{-0.024}$	$22.72^{+0.18}_{-0.31}$	$9.62^{+0.06}_{-0.07}$	$10.11^{+0.09}_{-0.11}$	$0.33^{+0.05}_{-0.06}$	$10.56^{+0.08}_{-0.10}$	$0.65^{+0.07}_{-0.08}$
0.35	-17.2	$20.124^{+0.013}_{-0.013}$	$20.331^{+0.008}_{-0.009}$	$20.613^{+0.007}_{-0.007}$	$20.715^{+0.010}_{-0.011}$	$21.13^{+0.27}_{-0.85}$	$8.74^{+0.01}_{-0.01}$	$8.16^{+0.14}_{-0.20}$	$-0.87^{+0.02}_{-0.02}$	$9.21^{+0.12}_{-0.16}$	$-0.55^{+0.07}_{-0.08}$
	-18.2	$20.454^{+0.013}_{-0.014}$	$20.709^{+0.010}_{-0.010}$	$20.998^{+0.009}_{-0.009}$	$21.111^{+0.011}_{-0.011}$	$21.68^{+0.12}_{-0.17}$	$9.07^{+0.01}_{-0.01}$	$9.33^{+0.11}_{-0.16}$	$-0.33^{+0.05}_{-0.06}$	$9.59^{+0.10}_{-0.14}$	$-0.20^{+0.06}_{-0.08}$
	-19.2	$20.797^{+0.015}_{-0.016}$	$21.093^{+0.011}_{-0.011}$	$21.402^{+0.010}_{-0.011}$	$21.529^{+0.013}_{-0.013}$	$22.27^{+0.09}_{-0.11}$	$9.42^{+0.02}_{-0.02}$	$9.93^{+0.10}_{-0.13}$	$0.15^{+0.06}_{-0.08}$	$10.12^{+0.10}_{-0.13}$	$0.27^{+0.07}_{-0.09}$
	-20.2	$21.073^{+0.027}_{-0.028}$	$21.406^{+0.016}_{-0.016}$	$21.743^{+0.013}_{-0.013}$	$21.898^{+0.016}_{-0.017}$	$22.81^{+0.08}_{-0.09}$	$9.69^{+0.03}_{-0.03}$	$10.46^{+0.09}_{-0.12}$	$0.59^{+0.07}_{-0.08}$	$10.62^{+0.09}_{-0.12}$	$0.71^{+0.08}_{-0.09}$
	-21.2	$21.257^{+0.059}_{-0.069}$	$21.693^{+0.025}_{-0.026}$	$22.110^{+0.016}_{-0.017}$	$22.329^{+0.024}_{-0.025}$	$23.20^{+0.14}_{-0.20}$	$9.88^{+0.06}_{-0.07}$	$10.72^{+0.10}_{-0.12}$	$0.83^{+0.07}_{-0.09}$	$11.05^{+0.10}_{-0.13}$	$1.10^{+0.09}_{-0.12}$
0.45	-17.6	$20.325^{+0.013}_{-0.014}$	$20.532^{+0.009}_{-0.009}$	$20.806^{+0.007}_{-0.007}$	$20.895^{+0.010}_{-0.011}$	$21.65^{+0.20}_{-0.37}$	$8.94^{+0.01}_{-0.01}$	$9.16^{+0.14}_{-0.20}$	$-0.48^{+0.06}_{-0.08}$	$9.69^{+0.12}_{-0.16}$	$-0.17^{+0.09}_{-0.11}$
	-18.6	$20.643^{+0.013}_{-0.014}$	$20.874^{+0.009}_{-0.010}$	$21.157^{+0.008}_{-0.008}$	$21.264^{+0.010}_{-0.010}$	$22.05^{+0.11}_{-0.15}$	$9.26^{+0.01}_{-0.01}$	$9.75^{+0.12}_{-0.16}$	$-0.02^{+0.07}_{-0.09}$	$10.00^{+0.12}_{-0.16}$	$0.14^{+0.09}_{-0.11}$
	-19.6	$20.923^{+0.018}_{-0.019}$	$21.202^{+0.010}_{-0.010}$	$21.530^{+0.008}_{-0.008}$	$21.692^{+0.013}_{-0.013}$	$22.32^{+0.06}_{-0.07}$	$9.54^{+0.02}_{-0.02}$	$10.09^{+0.12}_{-0.16}$	$0.29^{+0.07}_{-0.09}$	$10.21^{+0.11}_{-0.15}$	$0.37^{+0.08}_{-0.10}$
	-20.6	$21.184^{+0.026}_{-0.027}$	$21.528^{+0.013}_{-0.013}$	$21.901^{+0.011}_{-0.011}$	$22.094^{+0.015}_{-0.015}$	$22.81^{+0.09}_{-0.11}$	$9.80^{+0.03}_{-0.03}$	$10.51^{+0.10}_{-0.14}$	$0.66^{+0.07}_{-0.09}$	$10.70^{+0.11}_{-0.14}$	$0.80^{+0.08}_{-0.11}$
	-21.6	$21.348^{+0.085}_{-0.106}$	$21.822^{+0.042}_{-0.047}$	$22.270^{+0.028}_{-0.029}$	$22.520^{+0.022}_{-0.024}$	$22.99^{+0.13}_{-0.18}$	$9.97^{+0.08}_{-0.11}$	$10.62^{+0.10}_{-0.14}$	$0.78^{+0.07}_{-0.09}$	$10.93^{+0.11}_{-0.15}$	$1.01^{+0.09}_{-0.11}$
0.55	-18.6	$20.678^{+0.009}_{-0.009}$	$20.870^{+0.007}_{-0.007}$	$21.151^{+0.006}_{-0.006}$	$21.234^{+0.009}_{-0.009}$	$21.88^{+0.12}_{-0.17}$	$9.30^{+0.01}_{-0.01}$	$9.59^{+0.12}_{-0.17}$	$-0.09^{+0.06}_{-0.07}$	$9.86^{+0.11}_{-0.16}$	$0.06^{+0.07}_{-0.09}$
	-19.6	$20.981^{+0.011}_{-0.011}$	$21.237^{+0.008}_{-0.008}$	$21.544^{+0.006}_{-0.007}$	$21.660^{+0.008}_{-0.008}$	$22.49^{+0.06}_{-0.07}$	$9.60^{+0.01}_{-0.01}$	$10.27^{+0.11}_{-0.15}$	$0.43^{+0.08}_{-0.10}$	$10.40^{+0.11}_{-0.14}$	$0.52^{+0.08}_{-0.10}$
	-20.6	$21.235^{+0.019}_{-0.020}$	$21.559^{+0.010}_{-0.011}$	$21.920^{+0.007}_{-0.007}$	$22.071^{+0.009}_{-0.010}$	$22.92^{+0.04}_{-0.05}$	$9.85^{+0.02}_{-0.02}$	$10.72^{+0.11}_{-0.15}$	$0.82^{+0.09}_{-0.11}$	$10.81^{+0.11}_{-0.15}$	$0.90^{+0.09}_{-0.12}$
	-21.6	$21.511^{+0.038}_{-0.042}$	$21.901^{+0.021}_{-0.022}$	$22.309^{+0.013}_{-0.014}$	$22.482^{+0.015}_{-0.015}$	$23.29^{+0.07}_{-0.08}$	$10.13^{+0.04}_{-0.04}$	$11.07^{+0.12}_{-0.16}$	$1.16^{+0.10}_{-0.13}$	$11.22^{+0.12}_{-0.17}$	$1.28^{+0.10}_{-0.14}$
0.65	-18.5	$20.769^{+0.008}_{-0.008}$	$20.932^{+0.005}_{-0.005}$	$21.191^{+0.005}_{-0.005}$	$21.248^{+0.007}_{-0.007}$	$22.11^{+0.14}_{-0.22}$	$9.39^{+0.01}_{-0.01}$	$9.68^{+0.10}_{-0.13}$	$0.00^{+0.05}_{-0.06}$	$10.04^{+0.10}_{-0.13}$	$0.20^{+0.07}_{-0.08}$
	-19.5	$21.034^{+0.008}_{-0.008}$	$21.233^{+0.005}_{-0.005}$	$21.503^{+0.005}_{-0.005}$	$21.585^{+0.006}_{-0.006}$	$22.42^{+0.06}_{-0.08}$	$9.65^{+0.01}_{-0.01}$	$10.13^{+0.10}_{-0.13}$	$0.36^{+0.06}_{-0.07}$	$10.27^{+0.10}_{-0.14}$	$0.45^{+0.07}_{-0.09}$
	-20.5	$21.288^{+0.013}_{-0.013}$	$21.570^{+0.007}_{-0.007}$	$21.895^{+0.006}_{-0.006}$	$22.025^{+0.008}_{-0.008}$	$22.94^{+0.03}_{-0.04}$	$9.91^{+0.01}_{-0.01}$	$10.72^{+0.12}_{-0.16}$	$0.84^{+0.09}_{-0.11}$	$10.79^{+0.12}_{-0.16}$	$0.89^{+0.09}_{-0.12}$
	-21.5	$21.512^{+0.021}_{-0.023}$	$21.882^{+0.012}_{-0.012}$	$22.261^{+0.010}_{-0.010}$	$22.422^{+0.013}_{-0.013}$	$23.23^{+0.05}_{-0.06}$	$10.13^{+0.02}_{-0.02}$	$11.01^{+0.12}_{-0.17}$	$1.11^{+0.10}_{-0.13}$	$11.12^{+0.13}_{-0.18}$	$1.20^{+0.10}_{-0.14}$
0.75	-19.5	$21.021^{+0.009}_{-0.009}$	$21.235^{+0.005}_{-0.005}$	$21.517^{+0.005}_{-0.005}$	$21.607^{+0.007}_{-0.007}$	$22.55^{+0.06}_{-0.08}$	$9.64^{+0.01}_{-0.01}$	$10.21^{+0.11}_{-0.14}$	$0.40^{+0.07}_{-0.08}$	$10.36^{+0.11}_{-0.15}$	$0.51^{+0.08}_{-0.10}$
	-20.5	$21.257^{+0.014}_{-0.014}$	$21.556^{+0.007}_{-0.007}$	$21.882^{+0.006}_{-0.006}$	$22.016^{+0.008}_{-0.008}$	$23.05^{+0.04}_{-0.04}$	$9.88^{+0.01}_{-0.01}$	$10.79^{+0.12}_{-0.17}$	$0.88^{+0.10}_{-0.13}$	$10.88^{+0.12}_{-0.17}$	$0.96^{+0.10}_{-0.14}$
	-21.5	$21.511^{+0.023}_{-0.024}$	$21.890^{+0.012}_{-0.012}$	$22.263^{+0.010}_{-0.010}$	$22.422^{+0.012}_{-0.013}$	$23.35^{+0.07}_{-0.08}$	$10.13^{+0.02}_{-0.02}$	$11.09^{+0.13}_{-0.18}$	$1.18^{+0.10}_{-0.14}$	$11.25^{+0.13}_{-0.18}$	$1.31^{+0.11}_{-0.15}$
0.85	-20.0	$21.193^{+0.011}_{-0.011}$	$21.433^{+0.006}_{-0.007}$	$21.710^{+0.006}_{-0.006}$	$21.820^{+0.009}_{-0.010}$	$22.98^{+0.05}_{-0.06}$	$9.81^{+0.01}_{-0.01}$	$10.64^{+0.12}_{-0.17}$	$0.75^{+0.09}_{-0.12}$	$10.76^{+0.12}_{-0.17}$	$0.85^{+0.10}_{-0.13}$
	-21.0	$21.442^{+0.017}_{-0.018}$	$21.745^{+0.011}_{-0.011}$	$22.059^{+0.008}_{-0.009}$	$22.200^{+0.010}_{-0.010}$	$23.37^{+0.05}_{-0.06}$	$10.06^{+0.02}_{-0.02}$	$11.07^{+0.12}_{-0.17}$	$1.15^{+0.10}_{-0.14}$	$11.21^{+0.12}_{-0.18}$	$1.26^{+0.11}_{-0.15}$
	-22.0	$21.773^{+0.056}_{-0.064}$	$22.086^{+0.032}_{-0.034}$	$22.419^{+0.020}_{-0.021}$	$22.589^{+0.028}_{-0.029}$	$23.56^{+0.08}_{-0.10}$	$10.39^{+0.06}_{-0.06}$	$11.25^{+0.13}_{-0.18}$	$1.36^{+0.10}_{-0.13}$	$11.46^{+0.13}_{-0.18}$	$1.53^{+0.11}_{-0.15}$
0.95	-20.0	$21.318^{+0.009}_{-0.009}$	$21.513^{+0.005}_{-0.005}$	$21.734^{+0.005}_{-0.005}$	$21.808^{+0.007}_{-0.007}$	$22.83^{+0.07}_{-0.08}$	$9.94^{+0.01}_{-0.01}$	$10.45^{+0.12}_{-0.17}$	$0.67^{+0.08}_{-0.09}$	$10.62^{+0.13}_{-0.18}$	$0.78^{+0.09}_{-0.12}$
	-21.0	$21.520^{+0.016}_{-0.016}$	$21.784^{+0.010}_{-0.010}$	$22.071^{+0.006}_{-0.007}$	$22.197^{+0.010}_{-0.011}$	$23.29^{+0.04}_{-0.05}$	$10.14^{+0.02}_{-0.02}$	$11.03^{+0.13}_{-0.19}$	$1.13^{+0.10}_{-0.14}$	$11.13^{+0.13}_{-0.18}$	$1.21^{+0.11}_{-0.14}$
	-22.0	$21.713^{+0.038}_{-0.041}$	$22.084^{+0.019}_{-0.020}$	$22.422^{+0.018}_{-0.019}$	$22.594^{+0.030}_{-0.032}$	$23.45^{+0.08}_{-0.10}$	$10.33^{+0.04}_{-0.04}$	$11.15^{+0.13}_{-0.18}$	$1.27^{+0.10}_{-0.13}$	$11.36^{+0.13}_{-0.19}$	$1.43^{+0.11}_{-0.15}$

[a] Minimal estimate of IR luminosity and SFR from median-stack total flux $-\ 1\,\sigma$ bootstrapping error.

[b] Maximal estimate of IR luminosity and SFR from mean-stack total flux $+\ 1\,\sigma$ bootstrapping error.

Appendix: MIPS 24 μm stack images

Here we provide MIPS 24 μm median-stack and mean-stack images of 37 subsets of galaxies in our sample. The images are available in the electronic edition of the Journal.

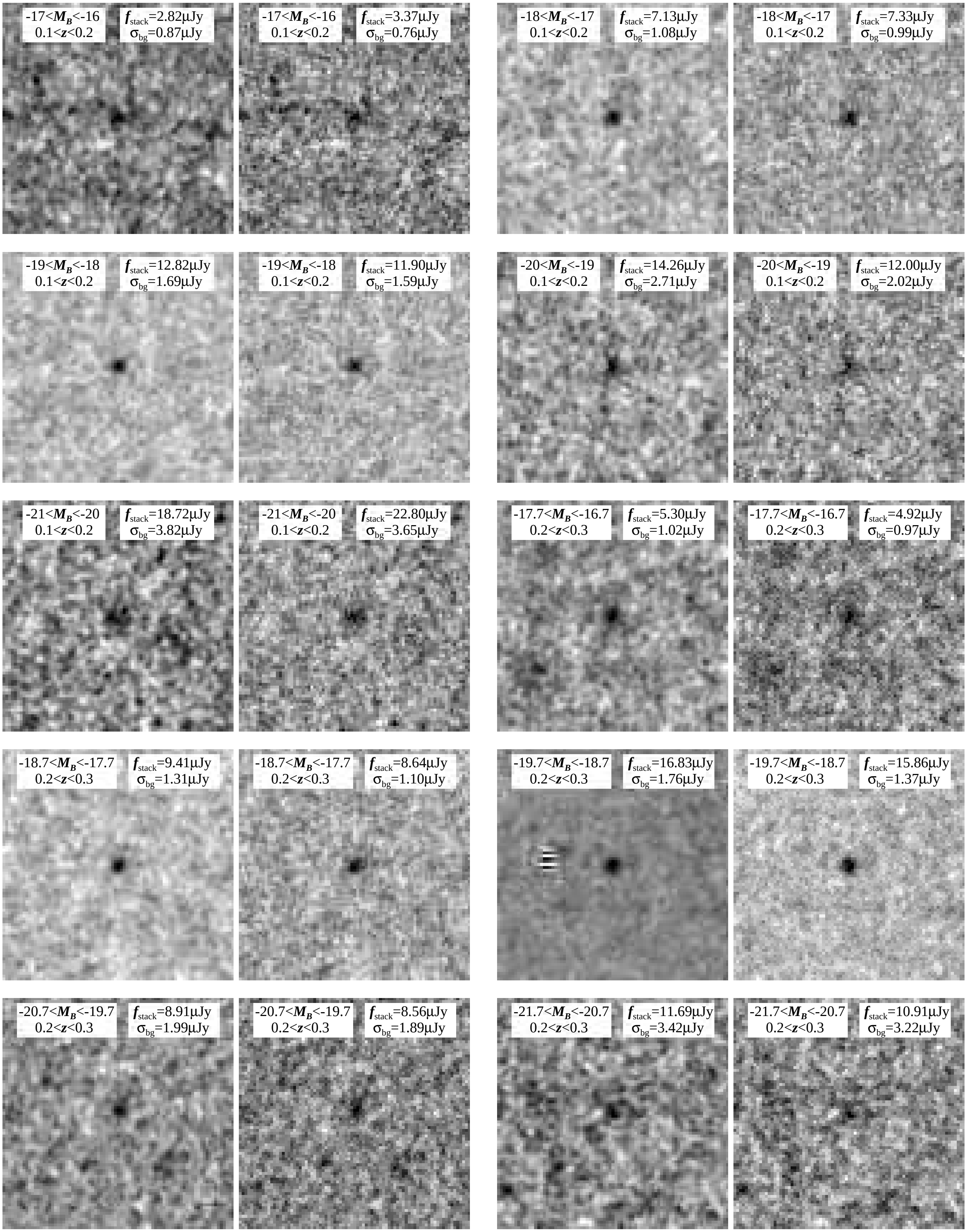
-17<M_B<-16 0.1<z<0.2 $f_{\rm stack}$=2.82μJy $\sigma_{\rm bg}$=0.87μJy
-17<M_B<-16 0.1<z<0.2 $f_{\rm stack}$=3.37μJy $\sigma_{\rm bg}$=0.76μJy
-18<M_B<-17 0.1<z<0.2 $f_{\rm stack}$=7.13μJy $\sigma_{\rm bg}$=1.08μJy
-18<M_B<-17 0.1<z<0.2 $f_{\rm stack}$=7.33μJy $\sigma_{\rm bg}$=0.99μJy
-19<M_B<-18 0.1<z<0.2 $f_{\rm stack}$=12.82μJy $\sigma_{\rm bg}$=1.69μJy
-19<M_B<-18 0.1<z<0.2 $f_{\rm stack}$=11.90μJy $\sigma_{\rm bg}$=1.59μJy
-20<M_B<-19 0.1<z<0.2 $f_{\rm stack}$=14.26μJy $\sigma_{\rm bg}$=2.71μJy
-20<M_B<-19 0.1<z<0.2 $f_{\rm stack}$=12.00μJy $\sigma_{\rm bg}$=2.02μJy
-21<M_B<-20 0.1<z<0.2 $f_{\rm stack}$=18.72μJy $\sigma_{\rm bg}$=3.82μJy
-21<M_B<-20 0.1<z<0.2 $f_{\rm stack}$=22.80μJy $\sigma_{\rm bg}$=3.65μJy
-17.7<M_B<-16.7 0.2<z<0.3 $f_{\rm stack}$=5.30μJy $\sigma_{\rm bg}$=1.02μJy
-17.7<M_B<-16.7 0.2<z<0.3 $f_{\rm stack}$=4.92μJy $\sigma_{\rm bg}$=0.97μJy
-18.7<M_B<-17.7 0.2<z<0.3 $f_{\rm stack}$=9.41μJy $\sigma_{\rm bg}$=1.31μJy
-18.7<M_B<-17.7 0.2<z<0.3 $f_{\rm stack}$=8.64μJy $\sigma_{\rm bg}$=1.10μJy
-19.7<M_B<-18.7 0.2<z<0.3 $f_{\rm stack}$=16.83μJy $\sigma_{\rm bg}$=1.76μJy
-19.7<M_B<-18.7 0.2<z<0.3 $f_{\rm stack}$=15.86μJy $\sigma_{\rm bg}$=1.37μJy
-20.7<M_B<-19.7 0.2<z<0.3 $f_{\rm stack}$=8.91μJy $\sigma_{\rm bg}$=1.99μJy
-20.7<M_B<-19.7 0.2<z<0.3 $f_{\rm stack}$=8.56μJy $\sigma_{\rm bg}$=1.89μJy
-21.7<M_B<-20.7 0.2<z<0.3 $f_{\rm stack}$=11.69μJy $\sigma_{\rm bg}$=3.42μJy
-21.7<M_B<-20.7 0.2<z<0.3 $f_{\rm stack}$=10.91μJy $\sigma_{\rm bg}$=3.22μJy

FIG. 12.— Median-stacked (left in a pair) and mean-stacked (right in a pair) MIPS 24 μm images for 37 stack bins in our sample. For each image, magnitude and redshift ranges are labeled at top-left; integrated central flux within aperture of radius 5″, $f_{\rm stack}$, and background RMS measured using the same aperture, $\sigma_{\rm bg}$, are labeled at top-right.

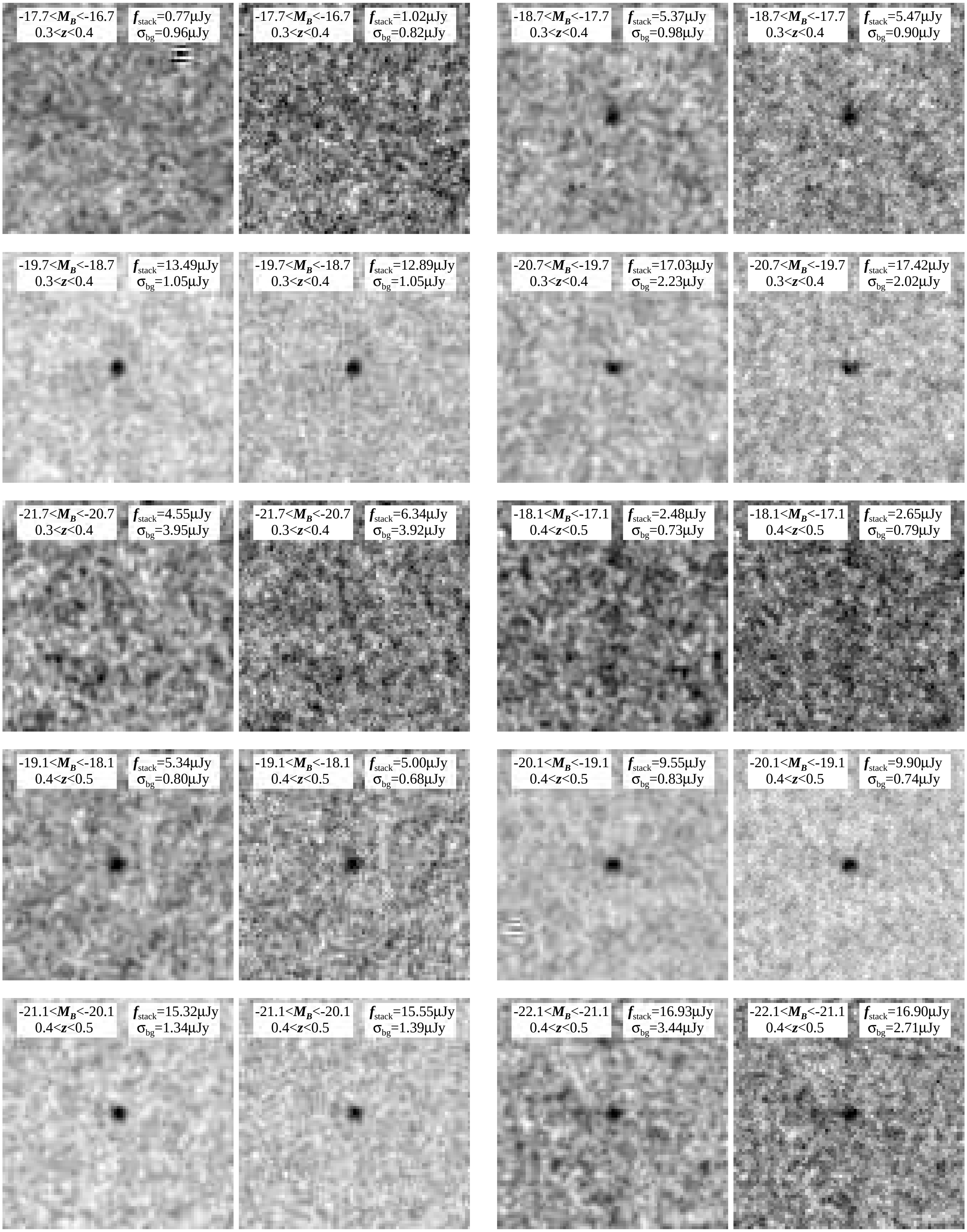
$-17.7<M_B<-16.7$ $0.3<z<0.4$
$f_{\rm stack}$=0.77μJy $\sigma_{\rm bg}$=0.96μJy
$-17.7<M_B<-16.7$ $0.3<z<0.4$
$f_{\rm stack}$=1.02μJy $\sigma_{\rm bg}$=0.82μJy
$-18.7<M_B<-17.7$ $0.3<z<0.4$
$f_{\rm stack}$=5.37μJy $\sigma_{\rm bg}$=0.98μJy
$-18.7<M_B<-17.7$ $0.3<z<0.4$
$f_{\rm stack}$=5.47μJy $\sigma_{\rm bg}$=0.90μJy
$-19.7<M_B<-18.7$ $0.3<z<0.4$
$f_{\rm stack}$=13.49μJy $\sigma_{\rm bg}$=1.05μJy
$-19.7<M_B<-18.7$ $0.3<z<0.4$
$f_{\rm stack}$=12.89μJy $\sigma_{\rm bg}$=1.05μJy
$-20.7<M_B<-19.7$ $0.3<z<0.4$
$f_{\rm stack}$=17.03μJy $\sigma_{\rm bg}$=2.23μJy
$-20.7<M_B<-19.7$ $0.3<z<0.4$
$f_{\rm stack}$=17.42μJy $\sigma_{\rm bg}$=2.02μJy
$-21.7<M_B<-20.7$ $0.3<z<0.4$
$f_{\rm stack}$=4.55μJy $\sigma_{\rm bg}$=3.95μJy
$-21.7<M_B<-20.7$ $0.3<z<0.4$
$f_{\rm stack}$=6.34μJy $\sigma_{\rm bg}$=3.92μJy
$-18.1<M_B<-17.1$ $0.4<z<0.5$
$f_{\rm stack}$=2.48μJy $\sigma_{\rm bg}$=0.73μJy
$-18.1<M_B<-17.1$ $0.4<z<0.5$
$f_{\rm stack}$=2.65μJy $\sigma_{\rm bg}$=0.79μJy
$-19.1<M_B<-18.1$ $0.4<z<0.5$
$f_{\rm stack}$=5.34μJy $\sigma_{\rm bg}$=0.80μJy
$-19.1<M_B<-18.1$ $0.4<z<0.5$
$f_{\rm stack}$=5.00μJy $\sigma_{\rm bg}$=0.68μJy
$-20.1<M_B<-19.1$ $0.4<z<0.5$
$f_{\rm stack}$=9.55μJy $\sigma_{\rm bg}$=0.83μJy
$-20.1<M_B<-19.1$ $0.4<z<0.5$
$f_{\rm stack}$=9.90μJy $\sigma_{\rm bg}$=0.74μJy
$-21.1<M_B<-20.1$ $0.4<z<0.5$
$f_{\rm stack}$=15.32μJy $\sigma_{\rm bg}$=1.34μJy
$-21.1<M_B<-20.1$ $0.4<z<0.5$
$f_{\rm stack}$=15.55μJy $\sigma_{\rm bg}$=1.39μJy
$-22.1<M_B<-21.1$ $0.4<z<0.5$
$f_{\rm stack}$=16.93μJy $\sigma_{\rm bg}$=3.44μJy
$-22.1<M_B<-21.1$ $0.4<z<0.5$
$f_{\rm stack}$=16.90μJy $\sigma_{\rm bg}$=2.71μJy

Fig. 12.— Continued.

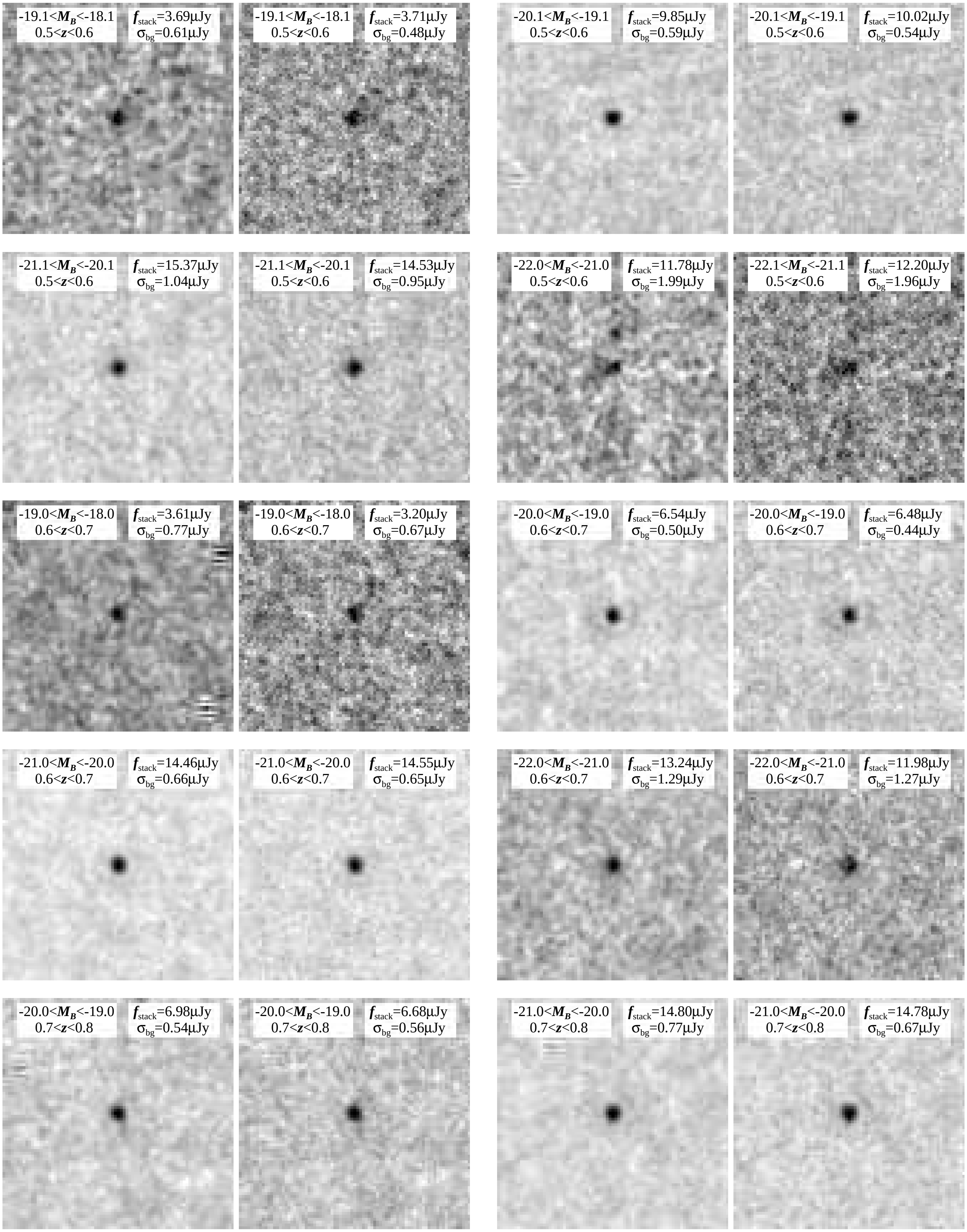
$-19.1<M_B<-18.1$ $0.5<z<0.6$
$f_{\rm stack}$=3.69μJy $\sigma_{\rm bg}$=0.61μJy
$-19.1<M_B<-18.1$ $0.5<z<0.6$
$f_{\rm stack}$=3.71μJy $\sigma_{\rm bg}$=0.48μJy
$-20.1<M_B<-19.1$ $0.5<z<0.6$
$f_{\rm stack}$=9.85μJy $\sigma_{\rm bg}$=0.59μJy
$-20.1<M_B<-19.1$ $0.5<z<0.6$
$f_{\rm stack}$=10.02μJy $\sigma_{\rm bg}$=0.54μJy
$-21.1<M_B<-20.1$ $0.5<z<0.6$
$f_{\rm stack}$=15.37μJy $\sigma_{\rm bg}$=1.04μJy
$-21.1<M_B<-20.1$ $0.5<z<0.6$
$f_{\rm stack}$=14.53μJy $\sigma_{\rm bg}$=0.95μJy
$-22.0<M_B<-21.0$ $0.5<z<0.6$
$f_{\rm stack}$=11.78μJy $\sigma_{\rm bg}$=1.99μJy
$-22.1<M_B<-21.1$ $0.5<z<0.6$
$f_{\rm stack}$=12.20μJy $\sigma_{\rm bg}$=1.96μJy
$-19.0<M_B<-18.0$ $0.6<z<0.7$
$f_{\rm stack}$=3.61μJy $\sigma_{\rm bg}$=0.77μJy
$-19.0<M_B<-18.0$ $0.6<z<0.7$
$f_{\rm stack}$=3.20μJy $\sigma_{\rm bg}$=0.67μJy
$-20.0<M_B<-19.0$ $0.6<z<0.7$
$f_{\rm stack}$=6.54μJy $\sigma_{\rm bg}$=0.50μJy
$-20.0<M_B<-19.0$ $0.6<z<0.7$
$f_{\rm stack}$=6.48μJy $\sigma_{\rm bg}$=0.44μJy
$-21.0<M_B<-20.0$ $0.6<z<0.7$
$f_{\rm stack}$=14.46μJy $\sigma_{\rm bg}$=0.66μJy
$-21.0<M_B<-20.0$ $0.6<z<0.7$
$f_{\rm stack}$=14.55μJy $\sigma_{\rm bg}$=0.65μJy
$-22.0<M_B<-21.0$ $0.6<z<0.7$
$f_{\rm stack}$=13.24μJy $\sigma_{\rm bg}$=1.29μJy
$-22.0<M_B<-21.0$ $0.6<z<0.7$
$f_{\rm stack}$=11.98μJy $\sigma_{\rm bg}$=1.27μJy
$-20.0<M_B<-19.0$ $0.7<z<0.8$
$f_{\rm stack}$=6.98μJy $\sigma_{\rm bg}$=0.54μJy
$-20.0<M_B<-19.0$ $0.7<z<0.8$
$f_{\rm stack}$=6.68μJy $\sigma_{\rm bg}$=0.56μJy
$-21.0<M_B<-20.0$ $0.7<z<0.8$
$f_{\rm stack}$=14.80μJy $\sigma_{\rm bg}$=0.77μJy
$-21.0<M_B<-20.0$ $0.7<z<0.8$
$f_{\rm stack}$=14.78μJy $\sigma_{\rm bg}$=0.67μJy

FIG. 12.— Continued.

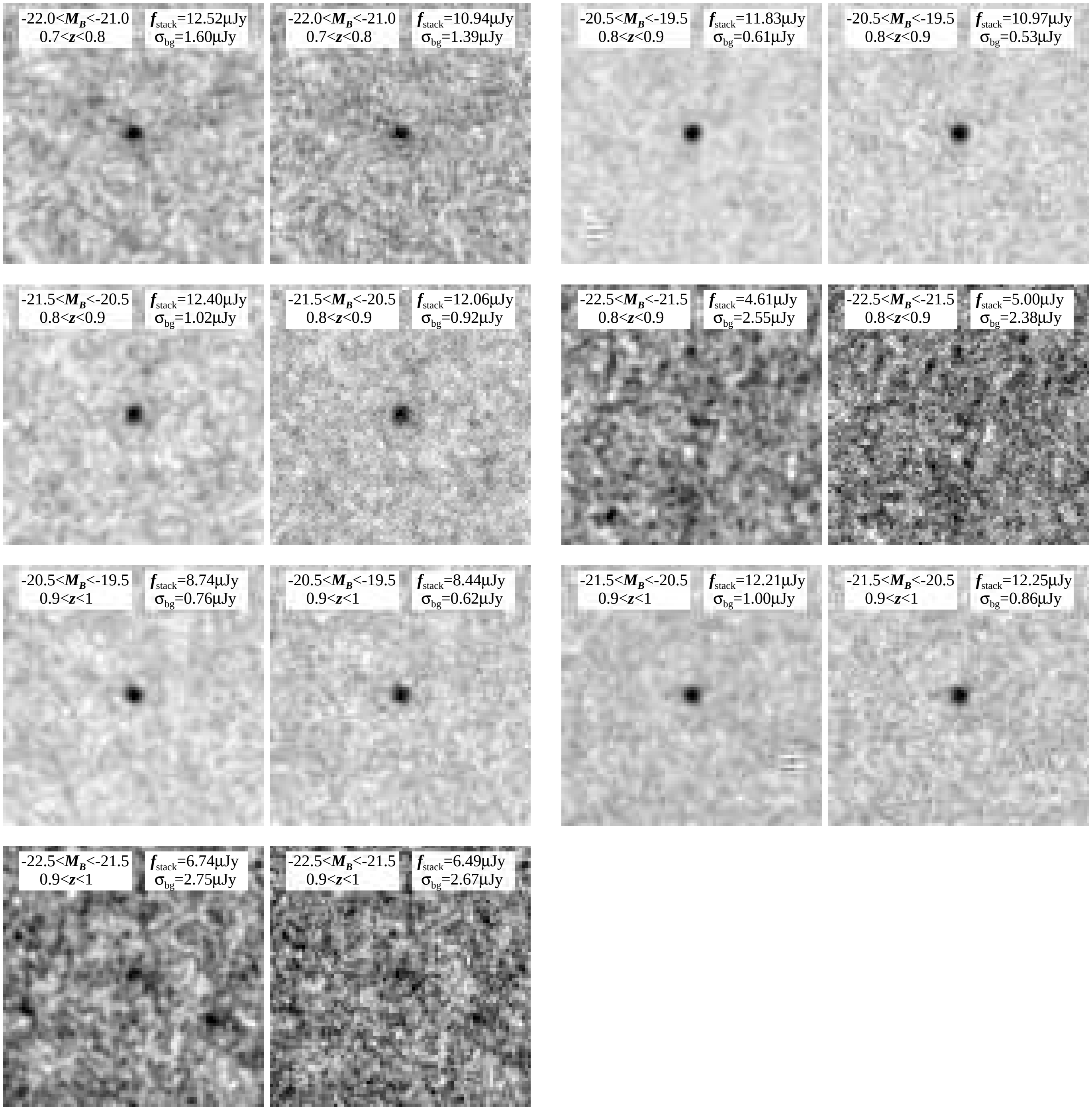
-22.0<M_B<-21.0 0.7<z<0.8 f_stack=12.52μJy σ_bg=1.60μJy
-22.0<M_B<-21.0 0.7<z<0.8 f_stack=10.94μJy σ_bg=1.39μJy
-20.5<M_B<-19.5 0.8<z<0.9 f_stack=11.83μJy σ_bg=0.61μJy
-20.5<M_B<-19.5 0.8<z<0.9 f_stack=10.97μJy σ_bg=0.53μJy
-21.5<M_B<-20.5 0.8<z<0.9 f_stack=12.40μJy σ_bg=1.02μJy
-21.5<M_B<-20.5 0.8<z<0.9 f_stack=12.06μJy σ_bg=0.92μJy
-22.5<M_B<-21.5 0.8<z<0.9 f_stack=4.61μJy σ_bg=2.55μJy
-22.5<M_B<-21.5 0.8<z<0.9 f_stack=5.00μJy σ_bg=2.38μJy
-20.5<M_B<-19.5 0.9<z<1 f_stack=8.74μJy σ_bg=0.76μJy
-20.5<M_B<-19.5 0.9<z<1 f_stack=8.44μJy σ_bg=0.62μJy
-21.5<M_B<-20.5 0.9<z<1 f_stack=12.21μJy σ_bg=1.00μJy
-21.5<M_B<-20.5 0.9<z<1 f_stack=12.25μJy σ_bg=0.86μJy
-22.5<M_B<-21.5 0.9<z<1 f_stack=6.74μJy σ_bg=2.75μJy
-22.5<M_B<-21.5 0.9<z<1 f_stack=6.49μJy σ_bg=2.67μJy

Fig. 12.— Continued.